Satellite Observations of Snowfall Regimes over the Greenland Ice Sheet

Elin A. McIlhattan[1], Claire Pettersen[2], Norman B. Wood[2], and Tristan S. L'Ecuyer[1]

[1]Department of Atmospheric and Oceanic Sciences, University of Wisconsin-Madison, Madison, Wisconsin, USA
[2]Space Science and Engineering Center, University of Wisconsin-Madison, Madison, Wisconsin, USA

Correspondence: Elin A. McIlhattan (mcilhattan@wisc.edu)

Abstract. The mass of the Greenland Ice Sheet (GIS) is decreasing due to surface melt and ice dynamics. Snowfall both adds mass to the GIS and has the capacity to reduce surface melt by increasing surface brightness, reflecting additional solar radiation back to space. Modeling the GIS's current and future mass balance and potential contribution to future sea level rise requires reliable observational benchmarks for current snowfall accumulation as well as robust connections between individual snowfall

5 events and the large-scale atmospheric circulation patterns that produce them. Previous work using ground-based observations showed that, for one research station on the GIS, two distinct snowfall regimes exist: those associated with exclusively ice-phase cloud processes (IC) and those involving mixed-phase processes indicated by the presence of super-cooled liquid water (CLW). The two regimes have markedly different accumulation characteristics and dynamical drivers. This study leverages the synergy between two satellite instruments, CloudSat's Cloud Profiling Radar (CPR) and CALIPSO's Cloud-Aerosol Lidar with Orthogonal Polarization (CALIOP), to identify snowfall cases over the full GIS and partition them into the IC and CLW

10 regimes. Overall, most CPR observations of snowfall over the GIS come from IC events (70 %), however, during the summer months, close to half of the snow observed is produced in CLW events (45 %). IC snowfall plays a dominant role in building the GIS, producing ∼80 % of the total estimated 399 Gt yr^{-1} accumulation. Beyond the cloud phase that defines the snowfall regimes, the macrophysical cloud characteristics are distinct as well; the mean IC geometric cloud depth (∼4 km) is consistently deeper than the CLW geometric cloud depth (∼2 km), consistent with previous studies based on surface observations. Two-

15 dimensional histograms of the vertical distribution of CPR reflectivities show that IC events demonstrate consistent growth toward the surface while CLW events do not. Analysis of ERA5 reanalyses shows that IC events are associated with cyclone activity and CLW events occur under large scale anomalous high pressure. Ground-based data is used to estimate the sensitivity of CloudSat's CPR to the two snowfall regimes, finding that the space-based radar is sensitive enough to detect ∼95 % of IC

20 snowfall cases and ∼75 % of CLW snowfall cases seen at the surface.

1 Introduction

The Greenland Ice Sheet (GIS) plays a key role in both the global energy budget (e.g. Box et al., 2012) and water cycle (e.g. Church et al., 2001; Enderlin et al., 2014). Unlike seasonally shifting sea-ice and snow cover, the GIS is a persistent bright surface, reflecting incoming solar energy back to space year-round. While there is variability in the percent of solar radiation

reflected by snow and ice surfaces (30-85 %) due to melt-refreeze events and the age of the snow cover (Noël et al., 2015), it is consistently higher than other high-latitude surfaces such as open ocean (<10 %), forests (10-25 %), or grasslands (15-30 %) (Petty, 2006). There is enough freshwater stored in the GIS to raise sea levels globally by 7.2 m (Church et al., 2001). Up until the 1990s, generally the mass gained from precipitation balanced the mass lost from melt runoff and ice dynamics in the

5   margins (Zwally et al., 2011; van den Broeke et al., 2016; Mouginot et al., 2019). However, in recent decades the GIS has been consistently losing mass (e.g. Zwally et al., 2011; van den Broeke et al., 2016; Mouginot et al., 2019; Mottram et al., 2019). Recent mass loss from the GIS has contributed 13.7 mm to global sea level rise (Mouginot et al., 2019) and the end of the century it is predicted to contribute up to 15 cm to the global mean sea level (Vaughan et al., 2013).

      Snowfall is responsible for both building mass and brightening the surface of the GIS. Surface brightness, or albedo, is
10   largely dependent on the frequency of precipitation because fresh snow is more reflective than old snow in the shortwave (SW) solar wavelengths (Petty, 2006; Box et al., 2012; Enderlin et al., 2014). However, the SW albedo only matters in summer when there is incoming solar radiation; therefore the seasonal timing of snowfall events must also be considered. Fresh snowfall in summer can reduce absorbed SW by up to a factor of ∼3, largely reducing local melt and meltwater runoff (Noël et al., 2015). Snowfall is the major source term for the mass of the GIS (Ettema et al., 2009; Bring et al., 2016), and in addition to frequency
15   the snowfall rate and duration of events are important for accumulation.

      Snowfall characteristics depend on atmospheric conditions, regional surface properties, and topography. There is consensus among modeling studies and observational datasets that most of the GIS snowfall is produced by cyclones, with the highest accumulation occuring where their moist air masses move up the steep orography of the southeastern coastline (e.g. Kapsner et al., 1995; Schuenemann et al., 2009; Hakuba et al., 2012; Vihma et al., 2016; Berdahl et al., 2018). One encounters less
20   agreement when it comes to the total amount of snowfall over the full GIS. Ground-based observations are concentrated near the coasts, and often indirectly measure snowfall using changes in surface height (Steffen and Box, 2001). Estimating snowfall frequency and accumulation over the whole ice sheet is often achieved using regional climate models (e.g. Berdahl et al., 2018; Mouginot et al., 2019) or reanalyses (e.g. Schuenemann et al., 2009). However, models and reanalyses require robust observations to serve as constraints, and since those are lacking, the community has produced a wide range of GIS snowfall
25   estimates (Vernon et al., 2013; van den Broeke et al., 2016).

      Given the scarcity of ground-based observations, satellites are needed to look at snowfall across the GIS. Surface snowfall can be estimated from space using brightness temperature depression in passive microwave measurements, however these estimates are subject to large errors when applied over non-ocean surfaces due to variations in surface emission (Liu and Curry, 1997), including emission variations of the ice and snow-covered surfaces of the GIS. Passive microwave sensors can
30   also provide information on the extent, and in some conditions depth, of the snowpack (Frei et al., 2012), however, they measure snow already on the ground which can be impacted by processes other than snowfall (e.g. blowing snow, melt events, etc) and do not give information about the clouds that produce the snow. Satellite-borne active sensors are currently the best platform to measure the annual cycle of snowfall over the full GIS and give insight into the coincident clouds. In recent years, the Cloud Profiling Radar (CPR) aboard NASA's CloudSat satellite has provided unprecedented insight into snowfall processes in
35   remote, ice-covered regions (e.g. Palerme et al., 2014; Norin et al., 2015; Palerme et al., 2016; Milani et al., 2018; Souverijns

et al., 2018; Palerme et al., 2019). Two recent studies have used CloudSat's CPR to look at snowfall over the GIS in particular: Lenaerts et al. (2019) focused on GIS snowfall frequency and leveraged the satellite observations to evaluate climate model output; and Bennartz et al. (2019) used the radar measurements to provide the first in-depth, observationally based snowfall rate estimates of the GIS.

5   In order to understand how snowfall on the ice sheet may change in the future, it is not sufficient to merely know how much snow accumulates but also understand the processes and large-scale drivers that produce it. Using detailed, ground-based measurements at Summit Station, a research facility in the center of the GIS, Pettersen et al. (2018) (hereafter P18) showed that there are distinct atmospheric processes associated with snowfall events that originate from either ice clouds or from Arctic mixed-phase clouds. P18 used microwave radiometers (MWRs) to partition snowfall events into the two regimes: those

10   produced by fully-glaciated ice clouds and those produced by Arctic mixed-phase clouds containing super-cooled liquid water (hereafter IC and CLW events, respectively). P18 highlighted that each precipitation regime exhibited marked differences in cloud microphysical properties, associated atmospheric circulations, and air mass origins.

P18 found that IC events at Summit are associated with deep clouds that advect moist air quickly up and over the southeast Greenland coastline and on to the central GIS. The North Atlantic cyclones that set up these cloud systems have been been

15   credited in many studies for producing snowfall over Greenland (e.g. Serreze and Barrett, 2008; Schuenemann et al., 2009; Berdahl et al., 2018). Conversely, P18 found that CLW events are associated with shallow clouds and slow-moving, quiescent air masses originating from the south and southwest coastlines. The high surface pressure anomaly associated with these conditions was shown by Hanna et al. (2016) to have mainly positive precipitation anomalies over the GIS in reanalyses. By dividing Summit snowfall by cloud phase, P18 illustrated that IC and CLW events at that particular location have distinct

20   large-scale dynamical drivers which may respond differently to the rapidly changing Arctic climate.

In this paper, we aim to expand the ground-based snowfall regime analysis of P18 to the full GIS, exploring the importance of cloud phase to both snowfall frequency and accumulation. Flying in the same NASA satellite constellation as CloudSat, the Cloud–Aerosol Lidar and Infrared Pathfinder Satellite Observations (CALIPSO) satellite carries the Cloud-Aerosol Lidar with Orthogonal Polarization (CALIOP) instrument which is highly sensitive to the cloud liquid layer at the top of Arctic

25   mixed-phase clouds and can thus reliably discern cloud phase (Matus and L'Ecuyer, 2017; McIlhattan et al., 2017; Morrison et al., 2018). In this work, we use cloud phase data from CALIOP to divide snowfall events identified by CloudSat's CPR into IC and CLW regimes. Leveraging the synergy of the two instruments, we:

- Quantify the percentage of IC and CLW events that are likely missed by CloudSat using ground-based instrumentation

- Map the seasonal frequency of snowfall over the GIS and show the relative contributions from IC and CLW events

30   - Quantify the total accumulation of snowfall and the fraction resulting from each regime

- Compare the satellite observations to ground-based data from Summit Station

- Examine the annual cycles of precipitation regimes and discuss their importance for building and brightening the GIS

- Document the average cloud properties of the two precipitation regimes and their full distributions

– Map the atmospheric circulations that favor each regime in different regions: near-Summit, southeastern, western, and northern GIS

In the following section we describe the datasets and methods used in this study (Section 2). In Section 3, we compare CloudSat's CPR to surface observations, showing that the CPR is capable of detecting ∼95 % of IC events and ∼75 % CLW

5   events. We go on to examine the distinctions between IC and CLW events in Section 4. Looking first at snowfall frequency and accumulation (Section 4.1), we find that the IC snowfall events are overall more frequent and have higher snowfall rates than the CLW events. IC snowfall therefore plays the dominant role in building the GIS, producing ∼80 % of the total annual accumulation. However, we find the CLW events to be nearly as frequent as IC events in the summer months, meaning that CLW events play an important role in brightening the GIS during the time of greatest solar insolation. We go on to examine

10 the differences in clouds characteristics for two regimes (Section 4.2). Clouds associated with IC snowfall are consistently both geometrically deeper and have larger integrated reflectivity values than clouds associated with CLW snowfall. The final distinction we look at is in atmospheric circulation patterns coincident with regime snowfall in four regions of the GIS (Section 4.3) We find evidence that varied cyclone locations are associated with IC events in each region, while CLW events in all regions occur under anomalously high pressure scenarios. We summarize our conclusions in Section 5.

15 ## 2   Datasets and Methods

To explore the connection between cloud phase and the rate and frequency of snowfall over the Greeland Ice Sheet (GIS), we used space-borne observations from NASA's A-Train satellite constellation. We employ a product developed using instruments at Summit Station as well as ground-based radar measurements to independently corroborate the regime behavior observed by the satellites. We leverage reanalysis output to investigate what large-scale atmospheric patterns are coincident with the two

20 precipitation regimes.

2.1   Satellite Data

NASA's A-Train satellites orbit at a height of 705 km and a 98.2° inclination in a sun-synchronous orbit, providing detailed observations of the atmosphere and underlying terrain from 82° S to 82° N (L'Ecuyer and Jiang, 2010). The CloudSat and CALIPSO satellites joined the A-Train in 2006 and their close positioning has allowed for over 10 years of collocated obser-

25 vations of the vertical distribution of clouds and precipitation. The 94-GHz CPR aboard CloudSat has a minimum detectable reflectivity factor of -30 dBZe and is sensitive to large cloud particles and hydrometeors (Tanelli et al., 2008). CALIPSO carries CALIOP (532- and 1064-nm wavelengths) which is capable of determining cloud phase based on the differing backscatter of ice crystals and liquid droplets (Wang et al., 2012). CALIOP's short wavelengths attenuate quickly and only penetrate clouds with relatively low optical depths, ∼3 or less (Chepfer et al., 2010), so CALIOP on its own is not capable of providing infor-

30 mation on moderate to heavy snowfall or snowfall beneath liquid cloud layers. The CPR's longer wavelength, however, can generally penetrate all Arctic clouds to detect underlying precipitation (Battaglia and Delanoë, 2013). It is the combined skill of these instruments that allows for this study.

CloudSat experienced a battery failure in 2011, causing the CPR to only provide data for daytime overpasses. Due to the high latitude position of the GIS, this malfunction has a seasonal impact, rather than a daily one. In summer, the GIS experiences nearly constant solar illumination so there is no difference in the pre- and post-2011 summertime data collection. While there is a reduction in the post-2011 wintertime Arctic data, it is not eliminated completely. The CPR continues to function for some
5 minutes as it passes into the darkness of boreal winter, resulting in the collection of approximately half of the wintertime Arctic observations collected prior to the battery malfunction (Skofronick-Jackson et al., 2019).

The satellite data used in this study is referred to in terms of overpasses and footprints. An overpass is an individual flyover of the GIS, and comes from a single granule of CloudSat data — one orbit around the Earth (roughly 1.5 hours). Each CloudSat footprint has a horizontal resolution of approximately 1.4 x 1.7 km at the surface. Because of its shorter wavelength, ~12
10 CALIOP footprints fit within a single CPR footprint. The CALIOP cloud phase information has therefore been scaled to the CPR resolution in the below described data products. In this study we use all available footprints where both the CPR and CALIOP were functioning. For the regional maps, all A-Train data were binned to a ~0.94° latitude by 1.25° longitude grid (consistent with McIlhattan et al. 2017).

This study is primarily based on three data products produced by the CloudSat Data Processing Center: 2C-SNOW-PROFILE,
15 2B-CLDCLASS-LIDAR, and 2B-GEOPROF (hereafter 2CSP, 2BCCL, and 2BG, respectively). These products have all been extensively described elsewhere so the reader is directed to the citations provided below for algorithm and validation details. All granules available in the R05 CloudSat data product release as of May 2019 are used - no years or months were excluded. In total this research includes more than 17 thousand overpasses of the GIS, consisting of 14.7 million total individual footprints, 2.4 million of which contained snowfall (Fig. 1). In addition to gridding the observations, we have also collected satellite
20 footprints made within each GIS drainage basin as defined by Zwally et al. (2012) and shown in Fig. 1. The basins each have consistent surface slope relative to atmospheric advection (Zwally et al., 2012), enabling us to look at snowfall characteristics in large regions that are more meaningfully homogeneous than grid boxes (Zwally et al., 2012).

The first step in our analysis is to obtain snowfall frequency and rate from 2CSP, a radar-only product that uses CPR reflectivity information from the lowest clutter free bin to estimate surface snowfall rates (Wood and L'Ecuyer, 2018). The
25 CPR cannot directly observe snowfall at the surface because of ground clutter — the bright surface return overwhelms the detector and creates a blind zone in the ~1-1.2 km closest to the surface. To make a surface rate estimation, 2CSP relies on the connection between precipitation-sized particles aloft and snowfall at the surface; the downward snow mass flux retrieved at the top of the blind zone is assumed to reach the surface (discussed in Section 3). Studies comparing 2CSP to surface data have validated this connection, specifically in the polar regions (Maahn et al., 2014; Milani et al., 2015; Norin et al., 2015; Palerme
30 et al., 2016). The minimum detectable rate for 2CSP is ~0.0005 mm/h.

We define a footprint as snowing if it has a non-zero 2CSP snowfall rate in the lowest clutter free bin, unless that bin is flagged as possibly contaminated by ground clutter. Potential contamination is indicated by the third bit in the 2CSP status flag, which is set when there is a large difference between the snowfall rate in the lowest clutter free bin and the bin immediately above. This occurs naturally if there is a very shallow snowfall event such as lake effect snow, where the precipitation-sized
35 particles are confined to ~1-1.5 km of the surface, or it means that lowest bin expected to be clutter free is actually contaminated

by surface return. Contamination is most prevalent in regions of steep, icy topography where the digital elevation map used to determine the surface level does not exactly match conditions at the time of the overpass (Bennartz et al., 2019). Palerme et al. (2019) showed that the edges of the GIS are particularly prone to clutter in the R04 version of 2CSP, but the updated elevation map in R05 has reduced the number of contaminated pixels. In this study we use the snowfall rate in the bin above the lowest for

5 all profiles with potential clutter contamination, consistent with Palerme et al. (2019) and Milani et al. (2018). Bennartz et al. (2019) also highlighted the issue of surface contamination in GIS snowfall estimates using 2CSP, but approached a solution by creating a completely new rate based on reflectivities aloft.

In a given footprint, if 2CSP indicates snowfall at the surface, we then obtain cloud phase for that footprint from the 2BCCL. The sensitivities of both the CPR and CALIOP are leveraged by 2BCCL to determine phase (Wang et al., 2012): the lidar is

10 particularly sensitive to cloud liquid layers while the CPR provides additional ice crystal information that the lidar may miss due to attenuation. 2BCCL gives each vertically contiguous cloud a single phase (ice, liquid, or mixed), regardless of how the particles within the cloud are distributed. If there are multiple cloud layers in a given column, we take the phase of the lowest cloud layer. Our liquid-containing classification (CLW) includes both 'liquid' and 'mixed' flags while our ice classification (IC) uses only 'ice'.

15 Finally, we use a second radar-only product, 2BG (Marchand et al., 2008), to further characterize the clouds producing snowfall by looking at reflectivity properties. From 2BG we obtain the height and magnitude of radar reflectivity factor, Ze, in the vertical column and also the vertically integrated reflectivity, Z_{path}, discussed below.

2.2 Z_{path}

Ice water path (IWP) is a useful measure to explore the contents of clouds, but converting radar reflectivities to IWP is sensitive

20 to ice habit and particle size distribution, which are quite variable over the GIS (P18; Korolev et al., 1999). In this work we use an alternate value, column-integrated reflectivity (Z_{path}, mm^6 m^{-2}). Z_{path} is a relatively simple measurement related to the amount of hydrometeor backscatter that can reliably be used as a proxy for IWP (defined as Z_{int} in Kulie et al., 2010; Pettersen et al., 2016). It is defined as:

$$Z_{path} = \int_{H_{CB}}^{H_{CT}} Z_{CPR}(z)dz,$$

(1)

25 with H_{CT} and H_{CB} as the cloud-top height and base, respectively, and Z_{CPR} is the CloudSat CPR radar reflectivity factor at a given height, z. Cloud boundaries come from 2BCCL and the reflectivities between those boundaries come from 2BG. The 2BG reflectivity factors are converted from the provided $dBZe$ to Ze before integrating, then from Z_{path} to $dB(Z_{path})$ for plotting and discussion (consistent with Kulie et al. (2010)).

2.3 Ground-based Data

The ground-based observations of snowfall, cloud phase, and radar reflectivity used in this study were collected as part of the ongoing Integrated Characterization of Energy, Clouds, Atmospheric State and Precipitation at Summit (ICECAPS) project (Shupe et al., 2013). Summit Station is located at 72°36' N, 38°25' W and is denoted with a white star on all GIS maps in this

5   work (e.g. Fig 1).

Surface detected snowfall events at Summit were defined and segregated into IC and CLW events using the novel method developed and detailed in P18. P18 leveraged differences in absorption and scattering properties of cloud liquid and ice in MWR measurements to separate the two precipitation regimes. The IC and CLW surface based snowfall data are for the period 2010-2015. The data product as well as technical details are available in the National Science Foundation Arctic Data Center

10   archive (Pettersen and Merrelli, 2018).

In Section 3, we use averaged reflectivity measurements from ICECAPS's millimeter wavelength cloud radar (MMCR) to estimate the detectability of surface snowfall events from space by the CPR. The MMCR is a vertically pointing, 35 GHz, Doppler pulsed radar (Moran et al., 1998) that is sensitive to both ice and liquid hydrometeors.

To convert the MMCR reflectivity native resolution to CloudSat-like footprints we use time averaging and thresholds that

15   closely mimic the CPR and its algorithm: a height range of 960-1200 m AGL, equivalent to the standard height of bin 5 of the CPR used in the 2CSP algorithm over land; and a time average of 300 s, which at a moderate wind speed of 5 m/s is equivalent to the horizontal CPR footprint of ∼1.5km. Missing MMCR reflectivites are excluded from the average, while clear bins are included.

The 1-minute resolution snowfall regime data (Pettersen and Merrelli, 2018) is sampled to match the MMCR time averaging

20   period. If snow occurred (defined in P18 as Precipitation Occurrence Sensor System (POSS) power unit >2) for any time during the sample, the sample counts as a snow occurrence, even if for the majority of the averaged time no snow was falling. For sample mean snowfall rates, the POSS rate was averaged over the sample with missing values omitted and values associated with POSS power unit <2 included as zeros.

2.4 Reanalyses

25   Similar to P18, in Section 4.3 we use reanalyses to examine the atmospheric circulations associated with IC and CLW events for various GIS regions. The European Centre for Medium-Range Weather Forecasts (ECMWF) provides the global reanalysis product ERA5 (C3S, 2017), from 1950 to present. ERA5 contains hourly data with a latitude and longitude spatial resolution of 0.25° x 0.25°.

For each region analyzed in Section 4.3, we use only the most intense 50 % of IC and 50 % of CLW events identified by

30   CloudSat/CALIPSO. To rank the strength of observed events, we take a cumulative sum of surface snowfall rate for a single overpass within a basin. Thus, both large-scale, light snowfall and small-scale, heavy snowfall are included in the top 50 %. For the selected events, we use the nearest hourly ERA5 output to examine the mean and anomaly of the 500 mb geopotential height (GPH) and winds. For the anomalies, we subtracted the long-term monthly mean from the event day/hour.

3 Quantifying Snowfall Detectability from Space

The ICECAPS instrument suite at Summit provides a unique opportunity to look at IC and CLW cases from both below and above. Radar-derived snowfall rate estimates are dependent on assumptions of ice habit, which is variable in space and time (Kulie et al., 2010), making it impossible to exactly measure surface snowfall from space. However, if the CPR detects
5 precipitation size particles immediately above the blind zone, it is a good indicator that snow is falling at the surface (Milani et al., 2018; Palerme et al., 2019; Bennartz et al., 2019).

When comparing 200 m and 700 m above ground level (AGL) snowfall reflectivities at Summit, Castellani et al. (2015) found evidence of growth — the reflectivities at 200 m AGL were larger than 700 m AGL on average — suggesting that towards the surface there is an increase in particle masses, an increase in number concentration, or a shift from small particles to large
10 particles in the size distribution (or a combination thereof). Since an increase in reflectivity can arise from one or more of these different processes, when we say "growth" throughout this work, we are not specifically implying particle mass increase, but the collection of snow property changes that can influence reflectivity. Castellani et al. (2015) showed the distribution of reflectivity differences between 200 and 700 m AGL have both positive and negative values, meaning that while on average snowflakes at the top of the blind zone likely underwent growth as they fell, it was not guaranteed. McIlhattan et al. (2017)
15 looked specifically at the presence of clouds containing super-cooled liquid over Summit and the frequency with which they precipitated, finding that the 2CSP and 2BCCL (R04 versions for 2007-10 only) matched well with the surface observations from Miller et al. (2015). Figure 6 of P18 further supports the idea that snowfall cases should be detectable from space, since reflectivities greater than 0 dBZ occur frequently above the blind zone: up to 3 km AGL for IC snowfall cases and 2 km AGL for CLW cases. However, the MMCR reflectivities shown in P18 cannot be directly compared to the CPR due to differing space
20 and time averaging.

Previous papers have mentioned that due to the blind zone of the CPR, a number of snowfall events are likely missed (e.g. Maahn et al., 2014; Palerme et al., 2019; Bennartz et al., 2019). We aim here to quantify that number for our two snowfall regimes. By averaging the Summit MMCR data for IC and CLW cases, we create a CPR-like vertical profile and use coincident POSS measurements to define cases as snowing or not. Averaging and instrument details can be found in Section
25 2.3. For profiles with snow occurrence, the sample is considered missed by the CloudSat-like MMCR observations if the radar reflectivity in the selected CloudSat vertical bin is below the -15 dBZe threshold as defined in the 2CSP algorithm. Despite the differing wavelengths of the CPR and MMCR (frequencies of 94 and 35 GHz, respectively), at the snowfall defining threshold of -15 dBZe their reflectivities are comparable. For such small reflectivities, in most cases the ice particles are small such that the reflectivity is in the Rayleigh regime for both wavelengths.
30 The results of this comparison are summarized in Table 1. Note that when the MMCR was averaged over time, sometimes more than one type of Summit snowfall event (IC, CLW, or indeterminate) were blended together. For clarity, we are only showing results for the combined total, IC-only, and CLW-only scenes. In IC-only averaged scenes, all included snowfall events contained only fully-glaciated ice clouds. In CLW-only averaged scenes, cloud liquid was present in each snow event, though to be clear the CLW clouds are almost always mixtures of both supercooled-liquid water and ice.

Out of 20,516 total snowfall events identified in the averaged P18 dataset, 22 % of the events would have been undetected by the CPR. When looking at the 9,777 CLW-only snowfall events, the missed fraction goes up to 25 % and for the 3,545 IC-only events the missed fraction goes down to 5 % (the remaining 7,194 cases are mixed or indeterminate). The mean snowfall rate reported by the P18 dataset for the missed events is consistently about half the rate of the detected cases, meaning that the CPR is missing the lighter of the events overall, and within both of the regimes. Broadly, these results indicate that the CPR is sensitive enough to detect nearly all of the IC-only cases (95 %) as they appear at Summit, but has more difficulty with the Summit CLW-only cases, capturing a smaller majority (75 %).

Bennartz et al. (2019) showed that 2CSP underestimates snowfall accumulation near Summit Station relative to stake field and MMCR estimates. P18 showed that CLW cases are responsible for slightly more than half of accumulation at Summit. Our results here indicate the CPR is likely missing ∼25 % of CLW cases, which could mean that the low 2CSP accumulation bias is an issue of missing snowfall cases entirely, rather than an underestimate of rate as was suggested in Bennartz et al. (2019). The following results are not modified based on this under-detection, but the implications are touched on in the discussion and conclusions.

4   IC and CLW Regime Characteristics

4.1   Snowfall Frequency and Accumulation

The frequency of snowfall varies both regionally and seasonally over the Greenland Ice Sheet (GIS). There is a north-south gradient in the annual frequency map of all snow events (Fig 2, a), with frequency increasing towards the southern end of the GIS. The highest concentration of snowfall observations is along the southeastern coastline. This is consistent with previously documented heavy snowfall in the area, with studies attributing it to the region's steep orography and interaction with paths of North Atlantic storms (e.g. Schuenemann et al., 2009; Hakuba et al., 2012; Berdahl et al., 2018). When we partition the annual snowfall into cases coincident with ice clouds (IC) and clouds containing liquid water (CLW) (Fig 2, b and c, respectively) the GIS snowfall frequency is clearly dominated by IC events. There is an east-west gradient in the regime fraction, with more CLW cases along the western side of the GIS than the eastern.

In wintertime (defined here as October through May, consistent with P18), there is very little snowfall in the northern GIS and an even stronger north-south gradient compared to the annual distribution (Fig 2, d). The concentration of events along the southeastern coastline is also more prominent, with snowfall occurring up to 40 % of the time. This is consistent with the wintertime high concentration of cyclone centers and increased cyclone intensity off the southeastern GIS coastline, found by Zhang et al. (2004) using reanalyses. IC events (Fig 2, e) make up nearly 100 % of the wintertime snowfall observations over most of the GIS, with the exception of western Greenland where CLW approaches 50 % of the cases in some grid boxes nearest the central coast (Fig 2, f).

In summertime (defined here as May through September, consistent with P18), the north-south gradient is gone, with a fairly consistent 20-30 % snowfall frequency over the GIS (Fig 2, g). The precipitation occurring at the edges and outside of the ice sheet is predominantly rainfall during this season, and since rain is excluded from this study the frequency over the coast

and ocean is reduced. CLW cases make up ∼50 % of the snowfall frequency over much of the ice sheet in summer months (Fig 2, i), which is consistent with what P18 observed at Summit Station. The southeastern coastline, however, remains more influenced by IC snowfall even in summer. The east-west gradient in regime fraction is distinct in summer, with more CLW along the western side of the ice sheet (reasons for this east-west regime divide are examined in Section 4.3). In the summer

5 months, the GIS receives ∼83 % of its annual incoming solar insolation. So while the IC events clearly occur more often annually, the CLW events are equally important for brightening the GIS and increasing the surface albedo during the months of intense downwelling shortwave radiation.

Snowfall accumulation is the only significant, positive term in the surface mass balance of the GIS (e.g Jakobson and Vihma, 2010; Zwally et al., 2011; Mottram et al., 2019). The estimate of mass added to the GIS by snowfall by season and regime is

10 shown in Fig 3. The mean annual accumulation for the study period is 399 Gt yr^{-1} (Fig 3, a) which is distributed nearly equally between winter (198 Gt yr^{-1}, Fig 3, d) and summer (201 Gt yr^{-1}, Fig 3, g). However, by our definition summer represents only five months compared to winter's seven, meaning that the intensity of summer snowfall is greater on average. Snowfall from IC events makes up ∼80 % of the total annual accumulation by mass, ∼88 % of the winter, and ∼71 % of the summer accumulation (Fig 3, b, e, and h, respectively). While there is some seasonal variation in the accumulation and distribution

15 between regimes, it is clear that in all basins the majority of the snowfall mass comes from IC events. The accumulation by individual basin is summarized in Table 2.

Previous estimates for GIS mean annual accumulation have generally been higher than this study, with different models, configurations, and reanalyses ranging from ∼581 - 899 Gt yr^{-1} (Cullather et al., 2014) and the recent CloudSat observational study, Bennartz et al. (2019), reported 586 ± 129 Gt yr^{-1}. As discussed previously, models and reanalyses rely on observations

20 for constraints, and over the GIS those have historically been sparse. The CPR derived snowfall rate in Bennartz et al. (2019) had a correction (relative to 2CSP) to increase high elevation rates to more closely match Summit observations with the assumption that there would be little effect outside of high elevations because snowfall was expected to be associated with higher reflectivities. While this is likely true for IC cases, the following analysis demonstrates that CLW clouds are consistently thinner geometrically and with low IWP over the full ice sheet. Our GIS accumulation estimate is likely biased low because

25 the CPR is missing ∼25 % of CLW snowfall cases (as discussed in Section 3), but it is not clear that tuning all high elevation snowfall rates to one particular location will improve our larger scale evaluation and thus we present 2CSP rates as they are.

A histogram of the rates for all observed snowfall (Fig. 4, a, top) illustrates that the vast majority (note the log scale on the y-axis) of snowfall observations are very light. Just over 92 % of the snowfall observed is contained in the first bin, which includes snowfall rates of ≤ 0.41 mm hr^{-1} liquid water equivalent. Snowfall is frequent in both seasons, with winter and summer time

30 periods each accounting for roughly half (∼1.2 million) of the snowfall-containing satellite footprints. The winter histogram (Fig. 4 b, top) looks much the same as the annual, though has slightly steeper drop-off from first to the second bin, indicating that winter snowfall is often lighter, fitting with the general scarcity of available atmospheric moisture during these months. The summer histogram (Fig. 4, c, top), on the other hand, shows a smaller decrease between the first and second bins, consistent with generally more summertime atmospheric moisture allowing for increased hydrometeor formation and/or growth. The slope of

35 the distributions between the two seasons is distinct, with summer having an overall steeper decline and fewer observations

over 6 mm hr^{-1} compared to winter. This means that while the common summer events are snowing at slightly higher rates on average, it is in winter that the less frequent, highest-intensity snowfall occurs. Jakobson and Vihma (2010) found a similar relationship using reanalysis data in the Arctic, showing winter having lower precipitation rates than summer overall, but the annual precipitation maximum occurring in winter along the southeastern GIS coastline. They attributed the regionally strong

5 winter snowfall to the strength and position of the North Atlantic cyclone tracks.

The distribution of snowfall events between the two regimes is stark. In the annual (Fig. 4, a, bottom), IC observations (red) are more frequent at all snow rates. The largest fraction of CLW events (blue, ∼32 %) occurs at the lightest snowfall rates and the fraction decreases rapidly, with all events greater than 6 mm hr^{-1} produced by ice clouds, consistent with the findings of P18 at Summit. In winter (Fig. 4, b, bottom) the CLW fraction decreases to ∼18 % for the lightest events and IC are responsible

10 for greater than 95 % of the observations of snowfall >2 mm hr^{-1}. CLW and IC produce nearly the same number of light events in summer (Fig. 4 c, bottom), and CLW has a larger share of the moderate events than in winter. However, in both summer and winter, the heaviest snowfall is produced by IC events.

The motivation for this study was to see if the analysis in P18 at Summit Station could be expanded to the full GIS, and if so, to see how the regime characteristics compare. To compare with the point source ground measurements from P18, we selected

15 only satellite observations made within 100 km of Summit Station (the starred circle in Fig 1). Fig 5 illustrates the annual cycle of regime cloud frequency: the fraction of IC events and the fraction of CLW events out of all the snowfall events observed. The CLW fraction for both the satellite (solid blue line) and the ground-based (dashed blue line) observations have close agreement, particularly in the summer months. The satellite CLW fraction is lower year round than the surface observations, which fits with the CPR missing ∼25 % of CLW events, as discussed in Section 3. The closer match between ground- and space-based

20 observed fractions in summer could be due to the higher cloud water content improving detectability from space. The IC events (red lines) from the two platforms follow a similar pattern in the summer months, though the ground-based fraction is smaller. During the winter there is a clear majority of near-Summit IC events observed from space. The surface observations, on the other hand, show a drop off in IC snow during winter, and at the same time have a minimum in CLW events. This results likely from the third, "indeterminate", category present in ground-based Summit observations in P18, but not in 2BCCL, being more

25 prevalent in winter.

A key takeaway of Fig 5, beyond general agreement between the two instrument platforms on the relative frequency of regimes, is the important role CLW events play in brightening and adding mass to the surface of the central ice sheet during the summer months. CLW events are roughly double the number of IC in July, and continue to dominate frequency in August, the highest month of accumulation at Summit (Bennartz et al., 2019).

30 ## 4.2 Cloud Characteristics

The annual cycle of geometric cloud depth for IC and CLW snowfall events (Fig 6, a) demonstrates that these regimes are consistently physically distinct in all months of the year. The CLW clouds are on average much shallower than the IC clouds, which is consistent with previous understanding of these regimes (e.g. Morrison et al., 2012; P18). The mean IC geometric depth hovers around 4 km with two broad maxima: one centered around January and one around August. The mean CLW

geometric depth is between 1.5 and 2.5 km, with a single peak in July-August. Looking at the monthly average and standard deviation (solid line and shaded region, respectively) for the full GIS, there is no overlap between the two regimes in any time of year.

Since the geometric cloud thickness is so distinct between the two regimes, it follows that the cloud water content will also

5 be different. In this work we use $dB(Z_{path})$ as a proxy for IWP (see method section 2.2). Looking at the annual cycle of $dB(Z_{path})$ for the full GIS (Fig. 6, b), the IC monthly averages show one main peak between May and October. IC $dB(Z_{path})$ has particularly small inter-annual variability June through September, the months with highest $dB(Z_{path})$. In contrast, the CLW $dB(Z_{path})$ has a broader and shallower summer peak and larger year to year variation (shown by the broader shaded region and spread of monthly markers) compared to IC events.

10 For the clouds observed within 100 km of Summit Station, the annual cycle shows that the IC events are consistently thicker geometrically than CLW events (Fig 7, a), though with more inter-annual variability compared to the full GIS (illustrated by the relatively larger shaded region) and no discernable annual cycle. Using ground based remote sensing, Miller et al. (2015) also found no clear annual cycle in integrated thickness for clouds above Summit Station. The near-Summit satellite observations of $dB(Z_{path})$ (Fig 7, b) have increased variability between years relative to the full GIS. Though the IC clouds still have higher

15 $dB(Z_{path})$ than CLW year round, both regimes have have much smaller monthly mean $dB(Z_{path})$ values near-Summit than for the full ice sheet. This implies decreased IWPs for both regimes near Summit relative to the rest of the GIS, consistent with the greater distance from moisture sources.

It is useful to look also at the distribution of individual snowfall events to understand the character of the clouds that make up the mean. The top row of Fig 8 is a collection of histograms containing all of the observed snowfall over the GIS for the

20 entire study period. From left to right we have: annual, winter, and summer time periods (a, b, and c, respectively). Overall, most observations of snowfall (70 %) over the GIS are coming from IC events; however, in the summer months, close to half (45 %) of the snow observed is produced in CLW events. Similar to the plot of the annual cycle, Fig 8, a, shows that overall IC and CLW snowfall event cloud have distinctly different geometric depths. However, the overlap in their distributions indicate that there are some individual IC events that are shallower and CLW that are deeper than is implied in the annual cycle plot.

25 Each regime histogram is individually normalized to better focus on and compare the shapes of the distributions, rather than the magnitudes. The CLW clouds are remarkably invariant across seasons, with a narrow distribution and a peak between 1 and 2 km in geometric thickness (Fig 8, b, c). The tail of the CLW distribution changes between winter and summer — summer has a longer tail to the right of the peak, responsible for the slight increase in mean thickness for those months seen in Fig 6, a. The IC clouds have a broader range of geometric depths than the CLW, with a wide peak in the annual distribution between

30 2 and 5 km geometric thickness that becomes slightly thinner in winter (2-4 km) and thicker in summer (3-6 km). There is also a change in the skewness of the distribution, with a positive skew (peak to the left, tail to the right) in the winter and a negative skew (peak to the right, tail to the left) in summer. The difference in the shapes of the distributions means that the average cloud depth does not shift as much between seasons as the peaks in the distribution would imply. The distribution of cloud depths near Summit (Fig 8, bottom row) are noisier, but demonstrate consistency with the full GIS results in both shape

35 and seasonal characteristics.

The histograms of $dB(Z_{path})$ (Fig. 9) demonstrate the distinct nature of the two regimes, with clear differences in the IC and CLW event distributions. The CLW events are again quite invariant between the annual, winter, and summer plots for both the full GIS (top) and within 100km of Summit (bottom). GIS-wide, the CLW has a sharp peak at $\sim$0 $dB(Z_{path})$, positive skew, and overall similarly shaped distributions during all three time periods. The GIS IC event distributions have broader peaks that are consistently at larger $dB(Z_{path})$ values than the CLW peak, and much higher values ($\sim$10 $dB(Z_{path})$) in summer. This indicates higher IWP year-round in the GIS IC snow events compared to CLW events, and an increased summer ice path for the IC events, coinciding with the peak in the annual cycle plot (6, b). The skewness of the IC events is again marked, with the annual having no strong skewness and winter and summer showing opposite skewness, positive and negative, respectively. This means that the $dB(Z_{path})$ of the most commonly present cloud (the mode) in the two seasons is more disparate than shown by the mean in the annual cycle. The near Summit distributions are again noisier compared to the full GIS, but are quite similar in overall behavior, though with relatively fewer values above $\sim$10 $dB(Z_{path})$.

Taking the cloud geometric thickness and $dB(Z_{path})$ together, another distinction becomes clear: the GIS CLW events exhibit relatively constant characteristics throughout the year, while the GIS IC events are more seasonally dependent, within limits. IC events have a distinct annual cycle for both cloud geometric depth and $dB(Z_{path})$, but the variability (shown by the shaded standard deviation) within that cycle is generally no larger than the CLW variability, and in the summer in particular the variation is smaller. The summertime $dB(Z_{path})$ increase in IC events is accompanied by only a small increase in geometric thickness, meaning the clouds are denser during this period.

While $dB(Z_{path})$ gives an estimate of the total ice content of a cloud, the distribution of that ice in the vertical profile can give insight into hydrometeor growth tendencies. As a reminder, by "growth" we refer to an increase in particle masses, an increase in number concentration, or a shift from small particles to large particles in the size distribution (or a combination thereof). Fig 10 contains two-dimensional (2D) histograms of CPR reflectivities as a function of height for each regime. The composite of all observed IC snow events (Fig 10, a) shows increasing reflectivity toward the surface, indicating growth from the top of the deep clouds moving down the column to the top of the blind zone. The IC histograms in the winter and summer (Fig 10, c and e, respectively) have narrower distributions for given heights compared to the annual, with generally higher reflectivities in summer but showing consistent growth patterns in both seasons.

The CLW snowfall does not have as defined a relationship between height and reflectivity (Fig 10, b), shown by the rounded distribution. The CLW winter and summer (Fig 10, d and f, respectively) histograms have similar, round distributions and reflectivity spreads, though the peak in height is slightly higher in winter ($\sim$2.5-3 km AGL) than in summer ($\sim$2 km AGL). Unlike the IC distribution, the CLW shape does not display a discernible growth pattern. Both the IC and CLW results are consistent with what P18 found using the MMCR from the ground.

4.3 Associated Atmospheric Circulations

The moisture required to produce GIS snowfall is not produced locally — evaporation over the snow- and ice-covered regions of the Arctic is negligible — so moisture must be imported from the lower latitudes (Jakobson and Vihma, 2010) and/or ice-free ocean surfaces during summer months. While there are certainly local factors to consider (topography, surface type, tempera-

ture, etc.), variations in atmospheric circulation have been determined to be the primary control on GIS snowfall accumulation (e.g. Alley et al., 1993; Kapsner et al., 1995; Chen et al., 1997). Knowing the large-scale meteorological conditions that are coincident with each snowfall regime can help better constrain both the present day mass balance of the GIS as well as predict how it might change in the future. In this section, we examine the atmospheric circulations associated with regime snowfall for

5 four GIS regions: near-Summit, southeastern, western, and northern.

First we look at near-Summit cases to find the coincident atmospheric conditions that are able to bring IC and CLW events all the way to the center of the GIS. To be included as a case for one of the regimes, an individual Summit overpass needed to contain a minimum of 10 contiguous snowfall footprints (equivalent to ∼15 km along-track) within 100 km of Summit Station, and of those footprints a minimum of 90 % had to be of that regime type. We then took only the strongest 50 % of the selected

10 overpasses (described in Section 2.4), giving 159 IC cases and 43 CLW near-Summit cases.

The mean 500mb geopotential heights (GPH) for near-Summit IC events (Fig. 11a) display a trough-ridge feature with a gradient bisecting the GIS. The mean winds close to Summit are coming from the south-southeast. The 500 mb GPH anomaly (Fig. 11c) shows a dipole with higher than average heights in the North Atlantic and lower than average over the western GIS and Baffin Bay. The anomalous winds are strong relative to the mean and come from the south-southeast. These conditions

15 are similar in character and magnitude to what P18 found when looking at IC events at Summit Station. The IC 500 mb mean and anomalous GPH patterns are consistent with low-level convergence advecting warm, moist air from the North Atlantic ocean surface vertically though the column and north over the steep southeast coast of Greenland. These conditions bear strong resemblance to synoptic conditions often credited with GIS snowfall (Chen et al., 1997; Serreze and Barrett, 2008; Rogers et al., 2004; Schuenemann et al., 2009).

20 The regional map of mean 500 mb GPH for near-Summit CLW cases (Fig. 11, b) indicates calm conditions, showing relatively uniform heights over the GIS and with low wind speeds around Summit coming from the south-southwest. The main feature of the CLW GPH anomaly (Fig. 11, d) is much higher than average heights over the entire GIS. Hanna et al. (2016) identified that persistent high pressure anomalies are consistent with increased GIS precipitation in reanalyses in the western and central regions. These CLW conditions are again consistent with what was found in P18. This overall picture of quiescent

25 flow and large-scale subsidence is known for maintaining Arctic mixed-phase clouds (Morrison et al., 2012). While in this work we are focused on precipitation production, it is worth noting that these conditions also have the potential to enhance melt over the GIS through radiative forcing (Van Tricht et al., 2016).

The strength of our satellite approach is that we can look beyond Summit station to extend the P18 surface-based analysis and examine conditions coincident with regime snowfall in areas without ground-based observatories. We start by looking at cases

30 of snowfall in the northern GIS, defined here as basins 1.1, 1.2, 1.3, and 1.4. Shupe et al. (2013) and Castellani et al. (2015) found essentially no snowfall at Summit associated with northerly surface wind components. Similarly, P18 saw negligible northerly surface winds with IC cases and a very small component for CLW cases, though northerly surface winds did occur outside of precipitation events. This hints that the air-masses responsible for northern GIS snowfall do not move on towards the central GIS.

Choosing the strongest 50 % of overpasses for each snowfall regime during the study period, we have 1,125 IC cases and 452 CLW cases making up the composite maps for the northern GIS (Fig. 12). There are more cases in the northern GIS than any other region we examine because of the concentration of satellite overpasses (see Fig. 1), not because it snows more frequently there. The IC mean 500 mb GPH map (Fig. 12, a) contains a trough to the west of the GIS and very calm upper level winds in

5 the northern GIS. The GPH anomaly map for IC cases (Fig. 12, c) has a dipole centered over the GIS with higher than average heights to the west of the GIS and a low centered on the northeastern coast, with the anomalous winds coming from the north into our basins of interest. In an analysis by Chen et al. (1997) looking at synoptic causes for GIS precipitation, it was found that high precipitation in the northern GIS in 1987-88 was associated with a mean cyclone located in the Arctic Ocean close to the northeast coast of Greenland. The low anomaly in IC 500 mb GPH seen in Fig. 12, c is suggestive of a mean cyclone in

10 that location.

The northern GIS CLW cases are associated with a markedly different circulation pattern. Much like the near-Summit CLW cases, the mean 500mb GPH for northern GIS CLW cases has relatively uniform heights and low wind speeds. There is a strong anomalous ridge centered over Baffin Bay extending over the full GIS in the GPH anomaly plot (Fig. 12, d), with high anomalous northerly winds similar to the IC cases. The high anomalous winds moving over the northern GIS are pointed

15 southeast towards the center of the ice sheet, however the actual mean wind speeds present there are very low and coming from the west, indicating the CLW snowfall travels west to east in this region. This fits with previously mentioned work that showed snowfall in the central GIS does not come from the north (Shupe et al., 2013; Castellani et al., 2015; P18).

The western GIS is defined in this work as basins 6.1, 6.2, 7.1, 7.2, 8.1, and 8.2. Its composite (Fig. 13) includes 999 IC cases and 372 CLW cases. Again the mean 500 mb GPH for IC shows a trough to the west of Greenland (Fig. 13, a) and the mean for

20 CLW is relatively flat (Fig. 13, b). The GPH anomalies for the IC cases again show a dipole, but in this case the high anomaly is now off the southeastern Greenland coastline and the low anomaly is west-northwest of Greenland. The location of the low is possibly suggestive of the mean cyclone found by Chen et al. (1997) located in Baffin Bay and which they connected with increased snowfall in the central west GIS. The western GIS CLW events are associated with the same relatively flat 500mb mean GPH and high anomaly over the GIS (Fig. 13, b and d) seen in the northern and near-Summit composites. The anomalous

25 high ridge and winds show on-shore flow in the central west GIS. In their work using reanalyses to look at Greenland blocking, Hanna et al. (2016) showed similar 500 mb GPH and wind speed anomaly plots to be associated with positive precipitation anomalies along the western coastline of Greenland.

Moving finally to the southeastern GIS, defined as basins 3.3, 4.1, 4.2, 4.3, and 5.0, the composites shown in Fig. 14 are made up of 422 IC cases and 114 CLW cases. For this region the IC mean 500 mb GPH (Fig. 14, a) shows the deepest trough of

30 the four regions, similarly placed to the west of Greenland but now extending all the way to the southern tip. This is consistent with previous studies connecting north Atlantic stormtracks to heavy precipitation in the southeastern GIS (e.g. Chen et al., 1997; Schuenemann et al., 2009; Vihma et al., 2016; Berdahl et al., 2018). The IC anomaly plot (Fig. 14, c) has a strong dipole with the trough just to the west of the southern tip of the GIS and the ridge centered just east of Iceland. The anomalous winds associated with the dipole are high and flowing from the North Atlantic onto the southeastern GIS. This scenario is suggestive

35 of lee cyclogenesis, where cyclones form in the lee of the topographic ridge running along the southern tip of Greenland

(Rogers et al., 2004; Schuenemann et al., 2009). Lee cyclogenesis has been found previously to correlate with precipitation in the southern region (Chen et al., 1997; Schuenemann et al., 2009). Indeed, Berdahl et al. (2018) found that the position of the Icelandic low is a determining factor in the amount of snowfall hitting the southeastern coastline, with up to a 40 % increase when the low is in its far west position, relative to its far east position. The CLW GPH mean (Fig. 14, b) has a very shallow

5   trough-ridge feature, in the same location but much less distinct than for the IC events. The CLW anomaly (Fig. 14, d) shows a dipole, but the low is now fully off the continent, and most of the GIS is under an anomalous high that is directing onshore flow from the North Atlantic into the southeastern GIS.

In all of these regional composites, there are common themes for both the IC and the CLW cases. For each region the two regimes are related to clearly distinct circulation patterns. The IC anomalies tend to have a trough and ridge dipole centered

10   around the particular region of interest with anomalous flow directed onshore into the region in a pattern that resembles previously identified cyclone activity. The 500 mb GPH anomalies for the CLW consistently show an anomalous ridge over the GIS, but centered in such a way that the anomalous winds are directing flow and moisture into the region from the nearest coastline. These results point to IC snowfall being consistently associated with cyclone activity while CLW snowfall occurs under quieter, high pressure scenerios that favor long lived Arctic mixed-phase clouds.

5   Conclusions

Using CloudSat and CALIPSO observations, we quantify the frequency and rate of snowfall over the Greenland Ice Sheet (GIS) associated with two distinct microphysical regimes: snowfall produced by fully glaciated clouds (IC) and snowfall produced by Arctic mixed-phase clouds containing super-cooled liquid water (CLW). Motivated by the results in P18, this study determines the relative contribution of the two precipitation regimes to the mass of the full GIS.

20   Comparisons with ground-based observations show that CloudSat's CPR is sensitive enough to detect most IC events (∼95 %) as defined at the surface. However the CPR struggles with the shallower CLW events, identifying a smaller fraction of those defined at the surface (∼75 %). These missed cases likely result in an overall underestimation of GIS snowfall accumulation, particularly for the CLW accumulation values. While a future satellite based measurement system may reduce the depth of the blind zone, these missed cases represent a persistent limitation for CloudSat's CPR.

25   We find that, in general, snowfall occurs most frequently along the steep orography of the GIS's southeastern coastline, and IC events make up the majority of annual snowfall frequency (∼70 %). Across the full GIS, IC snowfall is responsible for ∼80 % of the estimated annual 399 Gt yr^{-1} accumulation. The relative contributions of the two regimes vary by basin, but in all basins and seasons, IC dominates the snowfall mass.

CLW frequency peaks in summer, with ∼45 % of all GIS snowfall observations associated with liquid containing clouds

30   during this season. Looking at cases near Summit Station, we find that CLW are more frequent than IC in July and August, agreeing with data gathered from ground-based instrumentation (P18).

By looking at the synoptic conditions coincident with each regime, we find that the IC events in all regions appear to be associated with cyclones interacting with the GIS, while CLW events are coincident with anomalously high 500 mb geopotential

heights over the GIS. In all regions and for both IC and CLW events, the anomalous winds direct flow and moisture onto the GIS from the nearest coastline.

Snowfall over the GIS matters in the energy and water cycles because of the ability to add mass to the ice sheet and increase the surface albedo. With this work we show that during the 2007-16 period, IC events played the larger role in adding mass,

5 but CLW's increased prevalence in the summer months has led to a nearly equal role in freshening the surface. Noël et al. (2015) highlighted that modeled GIS surface melt is highly sensitive to snowfall representation, and in some situations, the local reduction in mass loss from melt is larger than the increase in mass from the snowfall itself. While not the focus of this work, it is important to remember that CLW events have the competing surface effects of enhancing albedo with snow while the liquid bearing clouds also trap additional terrestrial radiation, potentially enhancing melt (Van Tricht et al., 2016; McIlhattan

10 et al., 2017)

For nearly half a century, the GIS has experienced net mass loss (e.g. van den Broeke et al., 2016; Mottram et al., 2019; Mouginot et al., 2019). Snowfall is the only significant, positive contribution to the mass of the GIS, however accurately modeling the current and future GIS snowfall has been hampered by a lack of large-scale, long term observational benchmarks. The mean frequency and accumulation values in this study should not be viewed as a climatology, but as a snapshot of characteris-

15 tics in a rapidly changing Arctic. However, this snapshot is useful in that it provides insights into the character of present-day snow events across the ice sheet and the dominant synoptic patterns that produce them. Lenaerts et al. (2019) compared observations from CloudSat to present-day model representation of GIS snowfall frequency and used those results to interpret the relevance of model predicted changes in future precipitation frequency. Zappa et al. (2013) showed that climate models predict significant changes in both the paths and intensities of North Atlantic cyclones in response to climate change. Mapping

20 our regime based results onto such predicted changes may yield additional insights into how this important source of ice sheet mass may change in a warmer climate.

Data availability. The satellite derived data products used in this study (2C-SNOW-PROFILE, 2B-CLDCLASS-LIDAR, and 2B-GEOPROF) are publicly available from the CloudSat Data Processing Center: http://www.cloudsat.cira.colostate.edu/data-products

The ground-based show classification product used in this study is publicly available from the National Science Foundation Arctic Data

25 Center: https://doi.org/10.18739/A2R28Q (Pettersen and Merrelli, 2018)

The MMCR data are publicly available from the NOAA Earth Science Research Laboratory's anonymous FTP server at ftp://ftp1.esrl.noaa.gov, directory psd3/arctic/summit/mmcr/products

The reanalysis data used in this study is available from ECMWF: https://confluence.ecmwf.int/display/CKB/ERA5+data+documentation. Note: Neither the European Commission nor ECMWF is responsible for any use that may be made of the Copernicus Information or Data it

30 contains.

Appendix A: List of acronyms

A list of all acronyms used in this manuscript.

2BCCL	**2B-C**LD**CLASS-L**IDAR (cloud dataproduct)
2BG	**2B-G**EOPROF (reflectivity dataproduct)
2CSP	**2C-S**NOW-**P**ROFILE (snowfall dataproduct)
AGL	**A**bove **G**round **L**evel
CALIOP	**C**loud–**A**erosol **Li**dar with **O**rthogonal **P**olarization (aboard CALIPSO)
CALIPSO	**C**loud-**A**erosol **L**idar and **I**nfrared **P**athfinder **S**atellite **O**bservation
CLW	**C**loud containing **L**iquid **W**ater (refering to snowfall regime)
CPR	**C**loud **P**rofiling **R**adar (aboard CloudSat)
ECMWF	**E**uropean **C**entre for **M**edium-Range **W**eather **F**orecasts
GPH	**G**eo**p**otential **H**eight
GIS	**G**reenland **I**ce **S**heet
ICECAPS	**I**ntegrated **C**haracterization of **E**nergy, **C**louds **A**tmospheric State and **P**recipitation at **S**ummit
IC	**I**ce **C**loud (refering to snowfall regime)
IWP	**I**ce **W**ater **P**ath
MMCR	**M**illi**m**eter **W**avelength **C**loud **R**adar
MWR	**M**icro**w**ave **R**adiometer
P18	**P**ettersen et al. (20**18**)
POSS	**P**recipitation **O**ccurrence **S**ensor **S**ystem
SW	**S**hort**w**ave (radiation)

References

Alley, R. B., Meese, D. A., Shuman, C. A., Gow, A. J., Taylor, K. C., Grootes, P. M., White, J. W. C., Ram, M., Waddington, E. D., Mayewski, P. A., and Zielinski, G. A.: Abrupt increase in Greenland snow accumulation at the end of the Younger Dryas event, Nature, 362, 527–529, https://doi.org/10.1038/362527a0, 1993.

5 Battaglia, A. and Delanoë, J.: Synergies and complementarities of cloudsat-calipso snow observations, Journal of Geophysical Research Atmospheres, 118, 721–731, https://doi.org/10.1029/2012JD018092, 2013.

Bennartz, R., Fell, F., Pettersen, C., Shupe, M. D., and Schuettemeyer, D.: Spatial and temporal variability of snowfall over Greenland from CloudSat observations, Atmospheric Chemistry and Physics Discussions, 2019, 1–32, https://doi.org/10.5194/acp-2018-1045, https://www.atmos-chem-phys-discuss.net/acp-2018-1045/, 2019.

10 Berdahl, M., Rennermalm, A., Hammann, A., Mioduszweski, J., Hameed, S., Tedesco, M., Stroeve, J., Mote, T., Koyama, T., and McConnell, J. R.: Southeast Greenland Winter Precipitation Strongly Linked to the Icelandic Low Position, Journal of Climate, 31, 4483–4500, https://doi.org/10.1175/JCLI-D-17-0622.1, 2018.

Box, J. E., Fettweis, X., Stroeve, J. C., Tedesco, M., Hall, D. K., and Steffen, K.: Greenland ice sheet albedo feedback: Thermodynamics and atmospheric drivers, Cryosphere, 6, 821–839, https://doi.org/10.5194/tc-6-821-2012, 2012.

15 Bring, A., Fedorova, I., Dibike, Y., Hinzman, L., Mård, J., Mernild, S. H., Prowse, T., Semenova, O., Stuefer, S. L., and Woo, M.-K.: Arctic terrestrial hydrology: A synthesis of processes, regional effects, and research challenges, Journal of Geophysical Research: Biogeosciences, 121, 621–649, https://doi.org/10.1002/2015JG003131, https://agupubs.onlinelibrary.wiley.com/doi/abs/10.1002/2015JG003131, 2016.

C3S: ERA5: Fifth generation of ECMWF atmospheric reanalyses of the global climate, Copernicus Climate Change Service Climate Data Store (CDS), date of access = July 2019, 2017.

20 Castellani, B. B., Shupe, M. D., Hudak, D. R., and Sheppard, B. E.: The annual cycle of snowfall at Summit, Greenland, Journal of Geophysical Research: Atmospheres, 120, 6654–6668, https://doi.org/10.1002/2015JD023072, https://agupubs.onlinelibrary.wiley.com/doi/abs/10.1002/2015JD023072, 2015.

Chen, Q.-s., Bromwich, D. H., and Bai, L.: Precipitation over Greenland Retrieved by a Dynamic Method and Its Relation to Cyclonic Activity, Journal of Climate, 10, 839–870, https://doi.org/10.1175/1520-0442(1997)010<0839:POGRBA>2.0.CO;2, 1997.

25 Chepfer, H., Bony, S., Winker, D., Cesana, G., Dufresne, J. L., Minnis, P., Stubenrauch, C. J., and Zeng, S.: The GCM-Oriented CALIPSO Cloud Product (CALIPSO-GOCCP), Journal of Geophysical Research: Atmospheres, 115, https://doi.org/10.1029/2009JD012251, https://agupubs.onlinelibrary.wiley.com/doi/abs/10.1029/2009JD012251, 2010.

Church, J. A., Gregory, J. M., Huybrechts, P., Kuhn, M., Lambeck, K., Nhuan, M., Qin, D., and Woodworth, P. L.: Climate Change 2001: The Scientific Basis, chap. 11, pp. 639–693, Cambridge University Press, 2001.

30 Cullather, R. I., Nowicki, S. M. J., Zhao, B., and Suarez, M. J.: Evaluation of the Surface Representation of the Greenland Ice Sheet in a General Circulation Model, Journal of Climate, 27, 4835–4856, https://doi.org/10.1175/JCLI-D-13-00635.1, 2014.

Enderlin, E. M., Howat, I. M., Jeong, S., Noh, M.-J., van Angelen, J. H., and van den Broeke, M. R.: An improved mass budget for the Greenland ice sheet, Geophysical Research Letters, 41, 866–872, https://doi.org/10.1002/2013GL059010, http://doi.wiley.com/10.1002/2013GL059010, 2014.

Ettema, J., van den Broeke, M. R., van Meijgaard, E., van de Berg, W. J., Bamber, J. L., Box, J. E., and Bales, R. C.: Higher surface mass balance of the Greenland ice sheet revealed by high-resolution climate modeling, Geophysical Research Letters, 36, https://doi.org/10.1029/2009GL038110, https://agupubs.onlinelibrary.wiley.com/doi/abs/10.1029/2009GL038110, 2009.

Frei, A., Tedesco, M., Lee, S., Foster, J., Hall, D. K., Kelly, R., and Robinson, D. A.: A review of global satellite-derived snow products, Advances in Space Research, 50, 1007 – 1029, https://doi.org/https://doi.org/10.1016/j.asr.2011.12.021, http://www.sciencedirect.com/science/article/pii/S0273117711008611, 2012.

Hakuba, M. Z., Folini, D., Wild, M., and Schär, C.: Impact of Greenland's topographic height on precipitation and snow accumulation in idealized simulations, Journal of Geophysical Research: Atmospheres, 117, https://doi.org/10.1029/2011JD017052, https://agupubs.onlinelibrary.wiley.com/doi/abs/10.1029/2011JD017052, 2012.

Hanna, E., Cropper, T. E., Hall, R. J., and Cappelen, J.: Greenland Blocking Index 1851?2015: a regional climate change signal, International Journal of Climatology, 36, 4847–4861, https://doi.org/10.1002/joc.4673, https://rmets.onlinelibrary.wiley.com/doi/abs/10.1002/joc.4673, 2016.

Jakobson, E. and Vihma, T.: Atmospheric moisture budget in the Arctic based on the ERA-40 reanalysis, International Journal of Climatology, 30, 2175–2194, https://doi.org/10.1002/joc.2039, 2010.

Kapsner, W. R., Alley, R. B., Shuman, C. A., Anandakrishnan, S., and Grootes, P. M.: Dominant influence of atmospheric circulation on snow accumulation in Greenland over the past 18,000 years, Nature, 373, 52–54, https://doi.org/10.1038/373052a0, 1995.

Korolev, A. V., Isaac, G. A., and Hallett, J.: Ice particle habits in Arctic clouds, Geophysical Research Letters, 26, 1299–1302, https://doi.org/10.1029/1999GL900232, https://agupubs.onlinelibrary.wiley.com/doi/abs/10.1029/1999GL900232, 1999.

Kulie, M. S., Bennartz, R., Greenwald, T. J., Chen, Y., and Weng, F.: Uncertainties in Microwave Properties of Frozen Precipitation: Implications for Remote Sensing and Data Assimilation, Journal of the Atmospheric Sciences, 67, 3471–3487, https://doi.org/10.1175/2010JAS3520.1, 2010.

L'Ecuyer, T. and Jiang, J.: Touring the Atmosphere Aboard the A-Train, Physics Today, 63, https://doi.org/10.1063/1.3653856, 2010.

Lenaerts, J. T. M., Camron, M. D., and Kay, J. E.: Present-day and future Greenland Ice Sheet precipitation frequency from satellite observations and an Earth System Model, *in prep*, 2019.

Liu, G. and Curry, J.: Precipitation characteristics in Greenland-Iceland-Norwegian Seas determined by using satellite microwave data, Journal of Geophysical Research: Atmospheres, 102, 13 987–13 997, https://doi.org/10.1029/96JD03090, https://agupubs.onlinelibrary.wiley.com/doi/abs/10.1029/96JD03090, 1997.

Maahn, M., Burgard, C., Crewell, S., Gorodetskaya, I. V., Kneifel, S., Lhermitte, S., Van Tricht, K., and Van Lipzig, N. P. M.: How does the spaceborne radar blind zone affect derived surface snowfall statistics in polar regions?, Journal of Geophysical Research D: Atmospheres, 119, 13 604–13 620, https://doi.org/10.1002/2014JD022079, 2014.

Marchand, R., Mace, G. G., Ackerman, T., and Stephens, G.: Hydrometeor detection using Cloudsat - An earth-orbiting 94-GHz cloud radar, Journal of Atmospheric and Oceanic Technology, 25, 519–533, https://doi.org/10.1175/2007JTECHA1006.1, 2008.

Matus, A. V. and L'Ecuyer, T. S.: The role of cloud phase in Earth's radiation budget, Journal of Geophysical Research: Atmospheres, 122, 2559–2578, https://doi.org/10.1002/2016JD025951, https://agupubs.onlinelibrary.wiley.com/doi/abs/10.1002/2016JD025951, 2017.

McIlhattan, E. A., L'Ecuyer, T. S., and Miller, N. B.: Observational Evidence Linking Arctic Supercooled Liquid Cloud Biases in CESM to Snowfall Processes, Journal of Climate, 30, 4477–4495, https://doi.org/10.1175/JCLI-D-16-0666.1, 2017.

Milani, L., Porcù, F., Casella, D., Dietrich, S., Panegrossi, G., Petracca, M., and Sanò, P.: Analysis of long-term precipitation pattern over Antarctica derived from satellite-borne radar, The Cryosphere Discussions, 9, 141–182, https://doi.org/10.5194/tcd-9-141-2015, http://www.the-cryosphere-discuss.net/9/141/2015/, 2015.

Milani, L., Kulie, M. S., Casella, D., Dietrich, S., L'Ecuyer, T. S., Panegrossi, G., Porcù, F., Sanò, P., and Wood, N. B.: CloudSat snowfall estimates over Antarctica and the Southern Ocean: An assessment of independent retrieval methodologies and multi-year snowfall analysis, Atmospheric Research, 213, 121–135, https://doi.org/10.1016/j.atmosres.2018.05.015, 2018.

Miller, N. B., Shupe, M. D., Cox, C. J., Walden, V. P., Turner, D. D., and Steffen, K.: Cloud Radiative Forcing at Summit, Greenland, Journal of Climate, 28, 6267–6280, https://doi.org/10.1175/JCLI-D-15-0076.1, 2015.

Moran, K. P., Martner, B. E., Post, M. J., Kropfli, R. A., Welsh, D. C., and Widener, K. B.: An Unattended Cloud-Profiling Radar for Use in Climate Research, Bulletin of the American Meteorological Society, 79, 443–456, https://doi.org/10.1175/1520-0477(1998)079<0443:AUCPRF>2.0.CO;2, 1998.

Morrison, A. L., Kay, J. E., Chepfer, H., Guzman, R., and Yettella, V.: Isolating the Liquid Cloud Response to Recent Arctic Sea Ice Variability Using Spaceborne Lidar Observations, Journal of Geophysical Research: Atmospheres, 123, 473–490, https://doi.org/10.1002/2017JD027248, https://agupubs.onlinelibrary.wiley.com/doi/abs/10.1002/2017JD027248, 2018.

Morrison, H., de Boer, G., Feingold, G., Harrington, J., Shupe, M. D., and Sulia, K.: Resilience of persistent Arctic mixed-phase clouds, Nature Geoscience, 5, 11–17, https://doi.org/10.1038/ngeo1332, 2012.

Mottram, R., B. Simonsen, S., Hø yer Svendsen, S., Barletta, V., Sandberg Sø rensen, L., Nagler, T., Wuite, J., Groh, A., Horwath, M., Rosier, J., Solgaard, A., Hvidberg, C., and Forsberg, R.: An Integrated View of Greenland Ice Sheet Mass Changes Based on Models and Satellite Observations, Remote Sensing, 11, 2019.

Mouginot, J., Rignot, E., Bjørk, A. A., van den Broeke, M., Millan, R., Morlighem, M., Noël, B., Scheuchl, B., and Wood, M.: Forty-six years of Greenland Ice Sheet mass balance from 1972 to 2018, Proceedings of the National Academy of Sciences, 116, 9239–9244, https://doi.org/10.1073/pnas.1904242116, https://www.pnas.org/content/116/19/9239, 2019.

Noël, B., van de Berg, W. J., van Meijgaard, E., Kuipers Munneke, P., van de Wal, R. S. W., and van den Broeke, M. R.: Evaluation of the updated regional climate model RACMO2.3: summer snowfall impact on the Greenland Ice Sheet, The Cryosphere, 9, 1831–1844, https://doi.org/10.5194/tc-9-1831-2015, 2015.

Norin, L., Devasthale, A., L'Ecuyer, T. S., Wood, N. B., and Smalley, M.: Intercomparison of snowfall estimates derived from the CloudSat Cloud Profiling Radar and the ground-based weather radar network over Sweden, Atmospheric Measurement Techniques, 8, 5009–5021, https://doi.org/10.5194/amt-8-5009-2015, 2015.

Palerme, C., Kay, J., Genthon, C., L'Ecuyer, T., B. Wood, N., and Claud, C.: How much snow falls on the Antarctic ice sheet?, The Cryosphere, 8, https://doi.org/10.5194/tc-8-1577-2014, 2014.

Palerme, C., Genthon, C., Claud, C., Kay, J., B. Wood, N., and L'Ecuyer, T.: Evaluation of current and projected Antarctic precipitation in CMIP5 models, Climate Dynamics, 48, https://doi.org/10.1007/s00382-016-3071-1, 2016.

Palerme, C., Claud, C., Wood, N. B., L'Ecuyer, T., and Genthon, C.: How Does Ground Clutter Affect CloudSat Snowfall Retrievals over Ice Sheets?, IEEE Geoscience and Remote Sensing Letters, 16, 342–346, https://doi.org/10.1109/LGRS.2018.2875007, 2019.

Pettersen, C. and Merrelli, A.: Microwave radiometer snow categorization tool for Summit, Greenland, 2010 - 2015, Arctic Data Center, https://doi.org/10.18739/A2R28Q., 2018.

Pettersen, C., Bennartz, R., Kulie, M. S., Merrelli, A. J., Shupe, M. D., and Turner, D. D.: Microwave signatures of ice hydrometeors from ground-based observations above Summit, Greenland, Atmospheric Chemistry and Physics, 16, 4743–4756, https://doi.org/10.5194/acp-16-4743-2016, https://www.atmos-chem-phys.net/16/4743/2016/, 2016.

Pettersen, C., Bennartz, R., Merrelli, A. J., Shupe, M. D., Turner, D. D., and Walden, V. P.: Precipitation regimes over central Greenland inferred from 5 years of ICECAPS observations, Atmospheric Chemistry and Physics, 18, 4715–4735, https://doi.org/10.5194/acp-18-4715-2018, https://www.atmos-chem-phys.net/18/4715/2018/, 2018.

Petty, G. W.: A First Course in Atmospheric Radiation, Sundog Publishing, second edition edn., 2006.

Rogers, J. C., Bathke, D. J., Mosley-Thompson, E., and Wang, S.-H.: Atmospheric circulation and cyclone frequency variations linked to the primary modes of Greenland snow accumulation, Geophysical Research Letters, 31, https://doi.org/10.1029/2004GL021048, https://agupubs.onlinelibrary.wiley.com/doi/abs/10.1029/2004GL021048, 2004.

Schuenemann, K. C., Cassano, J. J., and Finnis, J.: Synoptic Forcing of Precipitation over Greenland: Climatology for 1961-99, Journal of Hydrometeorology, 10, 60–78, https://doi.org/10.1175/2008jhm1014.1, 2009.

Serreze, M. C. and Barrett, A. P.: The Summer Cyclone Maximum over the Central Arctic Ocean, Journal of Climate, 21, 1048–1065, https://doi.org/10.1175/2007JCLI1810.1, 2008.

Shupe, M. D., Turner, D. D., Walden, V. P., Bennartz, R., Cadeddu, M. P., Castellani, B. B., Cox, C. J., Hudak, D. R., Kulie, M. S., Miller, N. B., Neely, R. R., Neff, W. D., and Rowe, P. M.: HIGH AND DRY: New Observations of Tropospheric and Cloud Properties above the Greenland Ice Sheet, Bulletin of the American Meteorological Society, 94, 169–186, http://www.jstor.org/stable/26219494, 2013.

Skofronick-Jackson, G., Kulie, M., Milani, L., Munchak, S. J., Wood, N. B., and Levizzani, V.: Satellite Estimation of Falling Snow: A Global Precipitation Measurement (GPM) Core Observatory Perspective, Journal of Applied Meteorology and Climatology, 58, 1429–1448, https://doi.org/10.1175/JAMC-D-18-0124.1, 2019.

Souverijns, N., Gossart, A., Lhermitte, S., Gorodetskaya, I. V., Grazioli, J., Berne, A., Duran-Alarcon, C., Boudevillain, B., Genthon, C., Scarchilli, C., and van Lipzig, N. P. M.: Evaluation of the CloudSat surface snowfall product over Antarctica using ground-based precipitation radars, The Cryosphere, 12, 3775–3789, https://doi.org/10.5194/tc-12-3775-2018, https://www.the-cryosphere.net/12/3775/2018/, 2018.

Steffen, K. and Box, J.: Surface climatology of the Greenland Ice Sheet: Greenland Climate Network 1995?1999, Journal of Geophysical Research, 106, 33 951, https://doi.org/10.1029/2001JD900161, 2001.

Tanelli, S., Durden, S. L., Im, E., Pak, K. S., Reinke, D. G., Partain, P., Haynes, J. M., and Marchand, R. T.: CloudSat's Cloud Profiling Radar After Two Years in Orbit: Performance, Calibration, and Processing, IEEE Transactions on Geoscience and Remote Sensing, 46, 3560–3573, https://doi.org/10.1109/TGRS.2008.2002030, 2008.

van den Broeke, M. R., Enderlin, E. M., Howat, I. M., Kuipers Munneke, P., Noël, B. P. Y., van de Berg, W. J., van Meijgaard, E., and Wouters, B.: On the recent contribution of the Greenland ice sheet to sea level change, The Cryosphere, 10, 1933–1946, https://doi.org/10.5194/tc-10-1933-2016, https://www.the-cryosphere.net/10/1933/2016/, 2016.

Van Tricht, K., Lhermitte, S., Lenaerts, J. T. M., Gorodetskaya, I. V., L'Ecuyer, T. S., Noel, B., van den Broeke, M. R., Turner, D. D., and van Lipzig, N. P. M.: Clouds enhance Greenland ice sheet meltwater runoff, Nat Commun, 7, https://doi.org/10.1038/ncomms10266, 2016.

Vaughan, D., Comiso, J., Allison, I., Carrasco, J., Kaser, G., Kwok, R., Mote, P., Murray, T., Paul, F., Ren, J., Rignot, E., Solomina, O., Steffen, K., and Zhang, T.: Observations: Cryosphere, book section 4, pp. 317–382, Cambridge University Press, Cambridge, United Kingdom and New York, NY, USA, https://doi.org/10.1017/CBO9781107415324.012, www.climatechange2013.org, 2013.

Vernon, C. L., Bamber, J. L., Box, J. E., van den Broeke, M. R., Fettweis, X., Hanna, E., and Huybrechts, P.: Surface mass balance model intercomparison for the Greenland ice sheet, The Cryosphere, 7, 599–614, https://doi.org/10.5194/tc-7-599-2013, https://www.the-cryosphere.net/7/599/2013/, 2013.

Vihma, T., Screen, J., Tjernström, M., Newton, B., Zhang, X., Popova, V., Deser, C., Holland, M., and Prowse, T.: The atmospheric role in the Arctic water cycle: A review on processes, past and future changes, and their impacts, Journal of Geophysical Research G: Biogeosciences, 121, 586–620, https://doi.org/10.1002/2015JG003132, 2016.

Wang, Z., Vane, D., and Stephens, G.: Level 2 Combined Radar and Lidar Cloud Scenario Classification Product Process Description and Interface Control Document, NASA JPL CloudSat project document Version 1.0, 61 pp., 2012.

Wood, N. B. and L'Ecuyer, T. S.: Level 2C Snow Profile Process Description and Interface Control Document, Product Version, P1_R05, NASA JPL CloudSat project document revision 0, 26 pp., http://www.cloudsat.cira.colostate.edu/sites/default/files/products/files/2C-SNOW-PROFILE_PDICD.P1_R05.rev0_.pdf, 2018.

Zappa, G., Shaffrey, L. C., Hodges, K. I., Sansom, P. G., and Stephenson, D. B.: A Multimodel Assessment of Future Projections of North Atlantic and European Extratropical Cyclones in the CMIP5 Climate Models, Journal of Climate, 26, 5846–5862, https://doi.org/10.1175/JCLI-D-12-00573.1, https://doi.org/10.1175/JCLI-D-12-00573.1, 2013.

Zhang, X., Walsh, J. E., Zhang, J., Bhatt, U. S., and Ikeda, M.: Climatology and Interannual Variability of Arctic Cyclone Activity: 1948–2002, Journal of Climate, 17, 2300–2317, https://doi.org/10.1175/1520-0442(2004)017<2300:CAIVOA>2.0.CO;2, 2004.

Zwally, H. J., Li, J., Brenner, A. C., Beckley, M., Cornejo, H. G., Marzio, J. D., Giovinetto, M. B., Neumann, T. A., Robbins, J., Saba, J. L., Yi, D., and Wang, W.: Greenland ice sheet mass balance: Distribution of increased mass loss with climate warming; 2003-07 versus 1992-2002, Journal of Glaciology, 57, 88–102, https://doi.org/10.3189/002214311795306682, 2011.

Zwally, H. J., Giovinetto, M. B., Beckley, M. A., and Saba, J. L.: Antarctic and Greenland Drainage Systems, GSFC Cryospheric Sciences Laboratory, http://icesat4.gsfc.nasa.gov/cryo_data/ant_grn_drainage_systems.php, 2012.
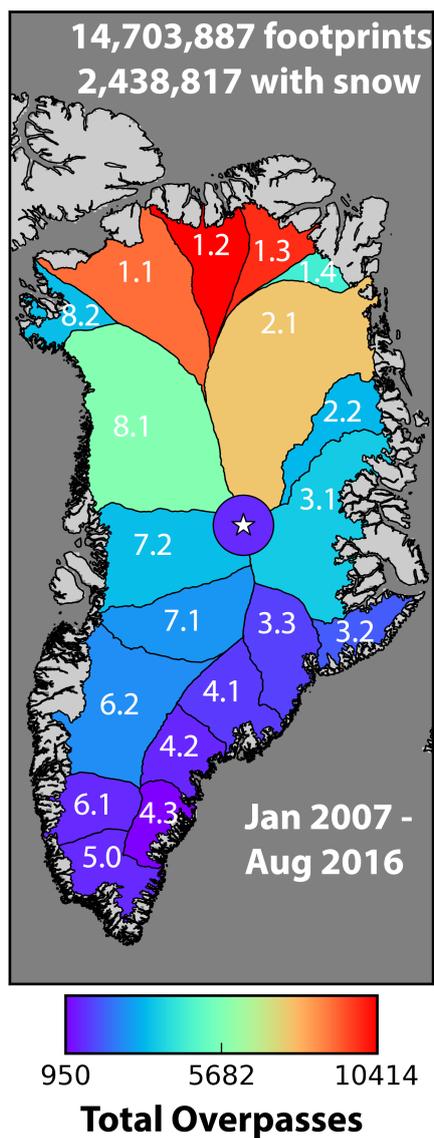
Figure 1. A summary of the CloudSat/CALIPSO satellite observations collected over the Greenland Ice Sheet (GIS). The GIS is divided into drainage basins as defined and numbered by the Ice Altimetry group at Goddard Space Flight Center. The color scale represents the total number of satellite overpasses in each basin during the full study period, January 2007 through August 2016. During that period, there were 14,703,887 individual satellite observations, 2,438,817 of which contained snowfall.
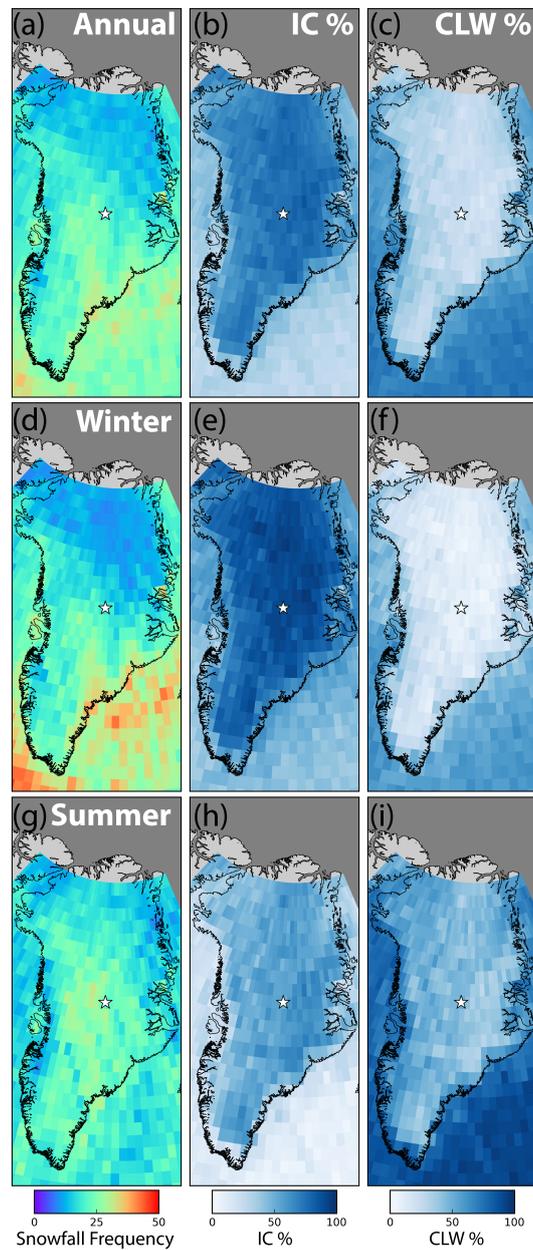
Figure 2. Snowfall frequency over the GIS defined as observations of snowfall divided by total observations in each gridbox. **(a)** is annual mean snowfall frequency using all observations from the study period, **(b)** is the percentage of total snowfall observations that were coincident with ice phase clouds, and **(c)** is the percentage of the total snowfall observations that were coincident with clouds containing liquid water. **(b)** and **(c)** sum to 100. **(d)** is winter mean snowfall frequency (Oct-Apr), with **(e)** and **(f)** the percentages of winter snowfall coincident with ice phase clouds and clouds containing liquid water, respectively. **(g)** is summer mean snowfall frequency (May-Sep), with **(e)** and **(f)** the percentages of summer snowfall coincident with ice phase clouds and clouds containing liquid water, respectively. The location of Summit Station is marked in each panel by a white star.
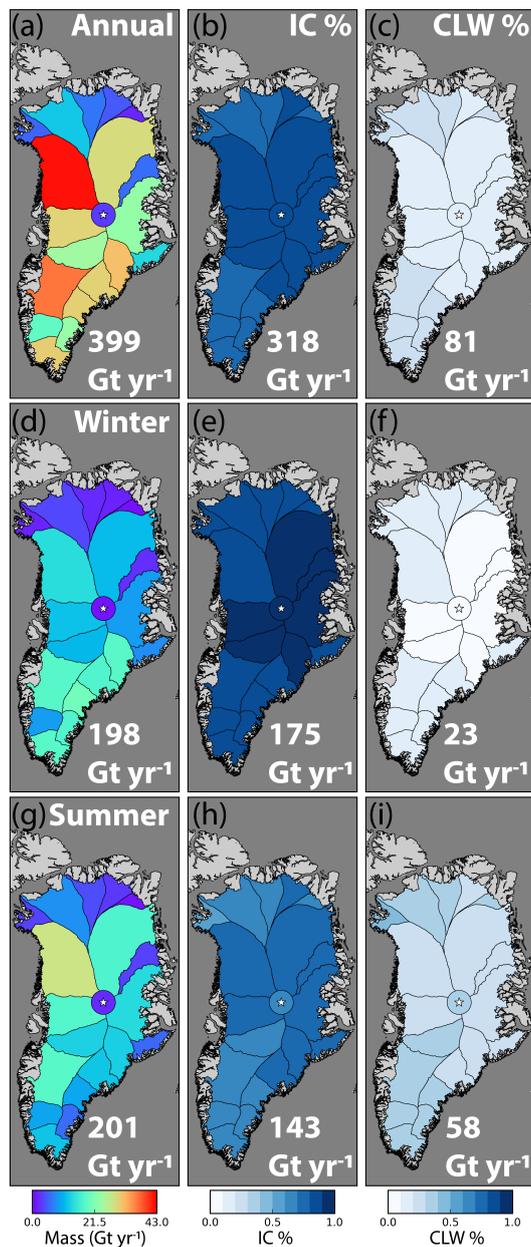
Figure 3. Snowfall mass contribution to the GIS. **(a)** is the annual average mass contribution broken down by basin, with the color scale representing Gt yr^{-1} for each basin and the total mass listed in the bottom left corner. **(b)** is the percentage of the snowfall mass produced by ice clouds, and **(c)** is the percentage of the mass produced by liquid containing clouds. The center (**(d)**, **(e)**, and **(f)**) and bottom (**(g)**, **(h)**, and **(i)**) rows are as the top row but for winter (Oct-Apr) and summer (May-Sep) months, respectively. The location of Summit Station is marked in each panel by a white star and the color of the circle surrounding it indicates the mass/percentage value for the area within 100km radius of the station.
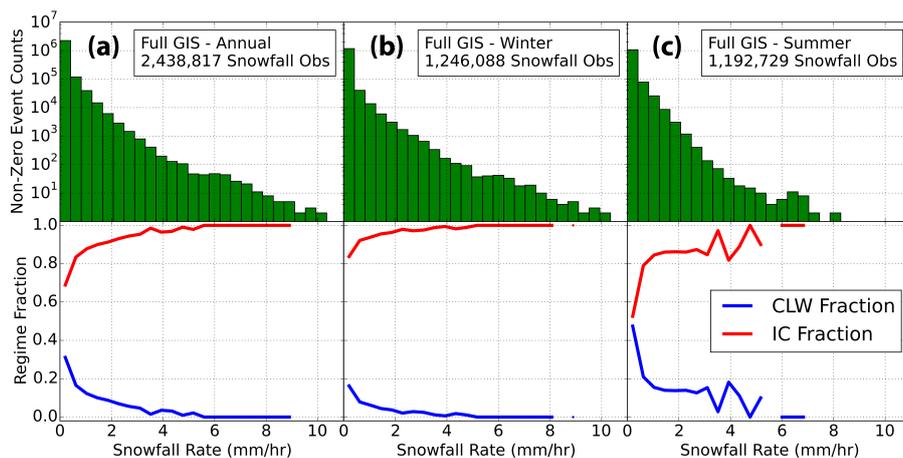
Figure 4. Snowfall rates for all observed snowfall. **(a)-top** is a histogram of the observed rates of all GIS snowfall from 2CSP (log scale), and **(a)-bottom** is the regime percent for each histogram bin. **(b)** and **(c)** are the same for GIS winter (Oct-Apr) and summer (May-Sep) months, respectively.
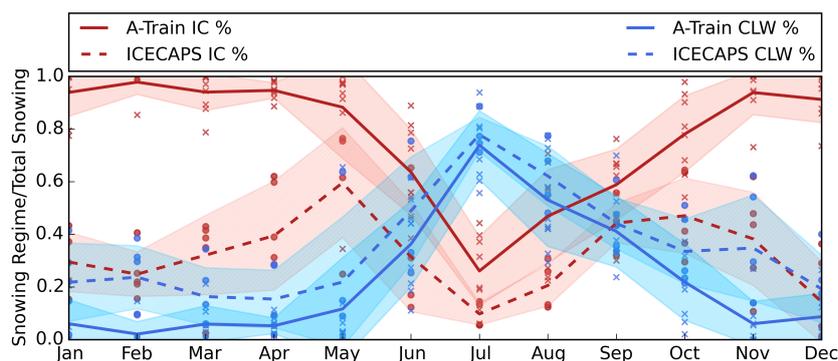
Figure 5. Annual cycle of regime fraction near Summit Station, Greenland. The regime fraction is the number of observations of one of the snowfall regimes (IC or CLW) divided by the total number of snowfall observations. A-Train values (solid lines, 'x' markers) shown for the near Summit annual cycle line plot are averages for all CPR footprints within 100km of Summit Station, Greenland. The solid lines represent the average of all observational years, each x depicting a single year's monthly average. The shaded region surrounding each line is the standard deviation about the mean for the month. The red color is for the IC regime percent and the blue is for the CLW regime percent. For the A-Train data, the red and blue add to 1.0. The ICECAPS values (dashed lines, circle markers) are from vertically pointing instruments at Summit Station, also with markers representing a single year's monthly average and the line being the mean of all years. The ICECAPS IC and CLW data do not add to 1.0 because of an additional category of 'indeterminate' (not plotted).
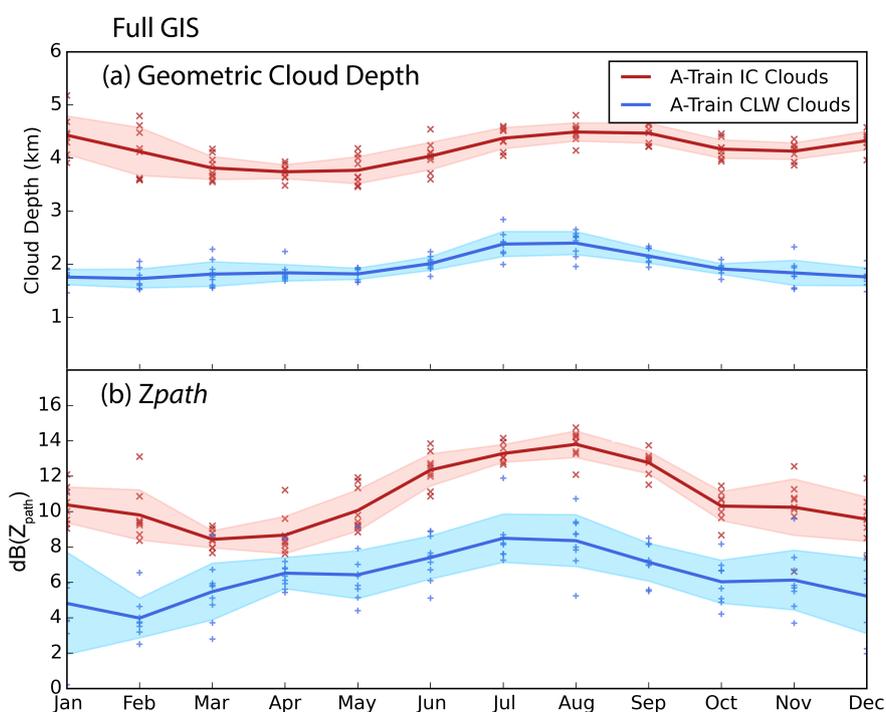
Figure 6. Annual cycle of GIS snowfall cloud characteristics. **(a)** the geometric cloud depth, and **(b)** the vertically integrated reflectivity for IC (red) and CLW (blue) snowfall observations. The solid lines represent the average of all observational years, each marker (x,+) depicting a single year's monthly average. The shaded region surrounding each line is the standard deviation about the mean for the month.
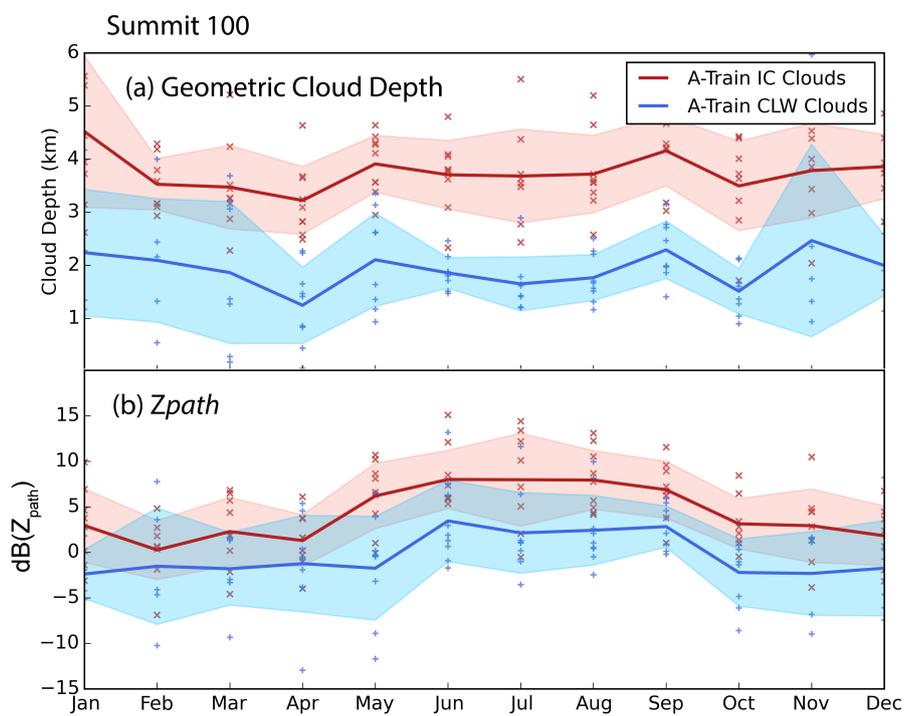
**Figure 7.** As in Fig 6 except only including observations within a 100 km radius of Summit Station.
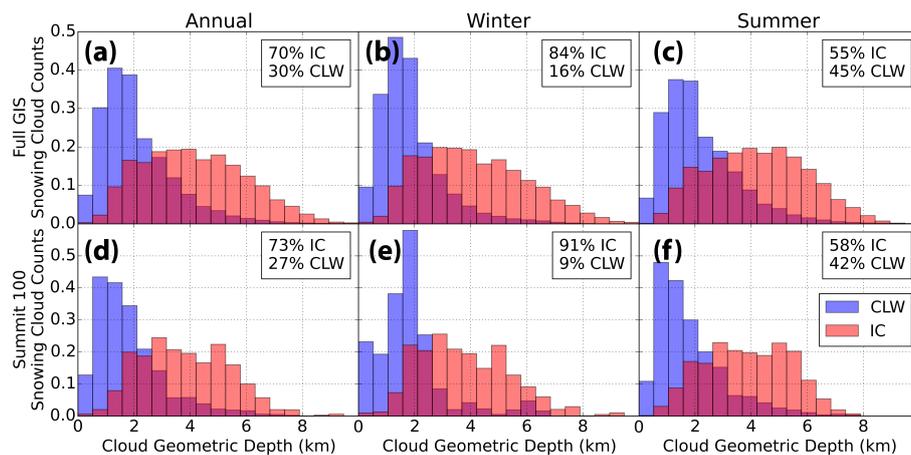
Figure 8. Histograms of precipitation regime geometric cloud depth. Red bins contain all footprints of IC snowfall and blue bins contain all footprints of CLW snowfall for each given season (Annual, Winter, and Summer) and region (Full GIS, Summit 100) as described in Fig 4. The histograms are normalized to highlight the distribution differences. The relative percentage of each regime is listed in the top right of each panel.
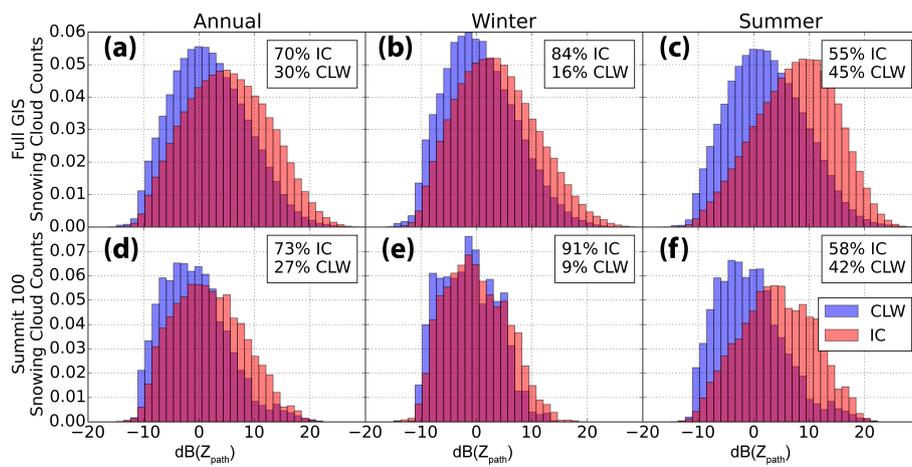
**Figure 9.** As in Fig 8 with $dB(Z_{path})$.
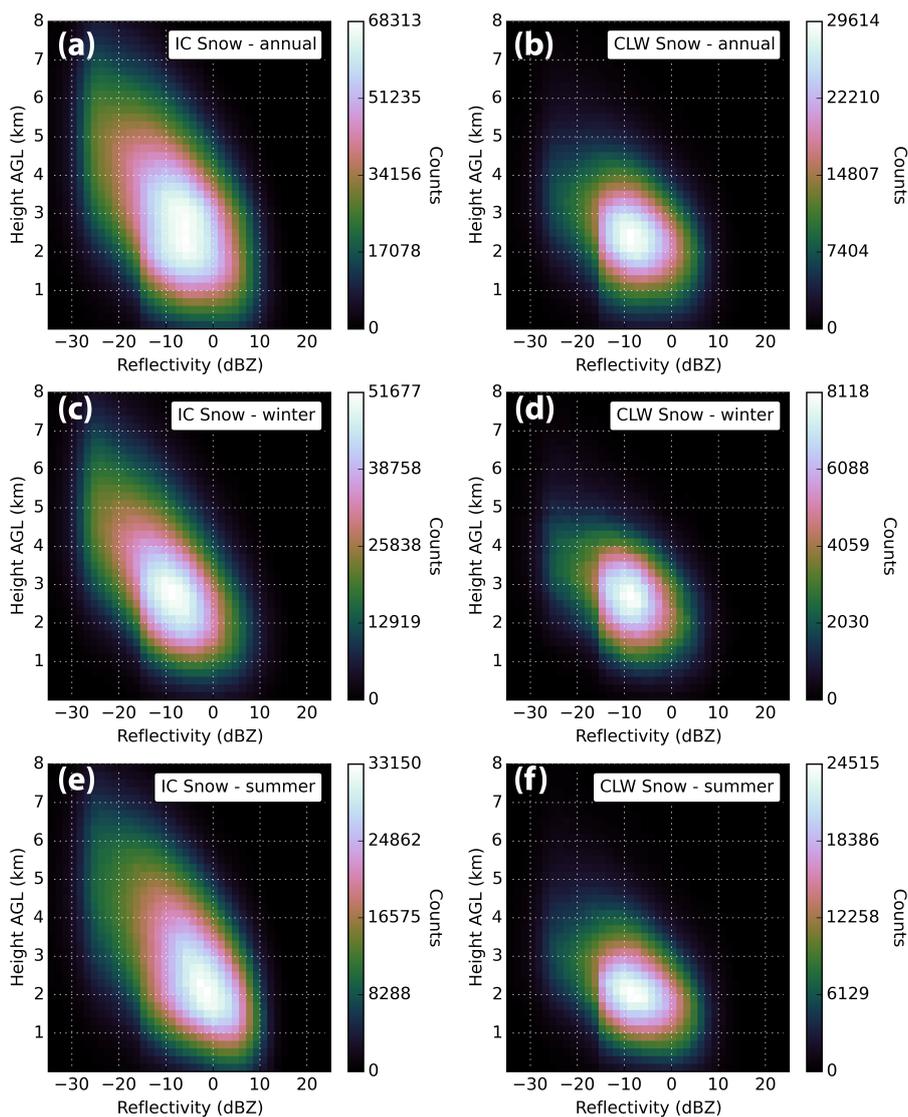
Figure 10. Composite two-dimensional histograms of CPR heights and reflectivities for the two snowfall regimes over the full GIS. The top row contains the entire annual cycle of events, including every footprint of snowfall detected during the study period, for IC **a)** and CLW **(b)** events. The center row contains all wintertime (Oct-Apr) IC **(c)** and CLW **(d)** events, and the bottom row contains all summertime (May-Sep) IC **(e)** and CLW **(f)** events. There is a discontinuity apparent in each panel at $\sim$-15 $dBZe$. This is due to the 2CSP threshold of -15 $dBZe$ for defining snowfall events. The shape and character of these plots compare well to P18 Fig. 6.
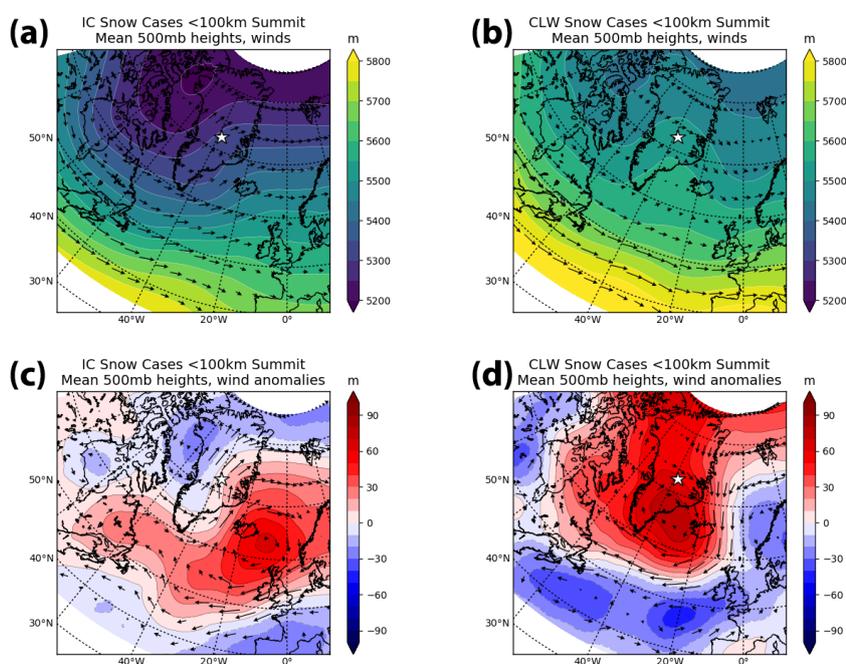
Figure 11. ERA5 derived mean and anomaly 500 mb geopotential heights (GPH) and winds for the strongest 50 % of precipitation events that occurred within a 100 km radius of Summit Station during the study period. **(a)** shows the average 500 mb GPH and winds for 159 IC events and **(b)** shows the same for 43 CLW events. **(c)** and **(d)** show the GPH and wind anomalies for the IC and CLW cases, respectively. These panels are all consistent with P18 Fig. 11, which also shows a strong trough ridge for the IC snow cases and relatively calm, quiescent conditions for the CLW snow cases.
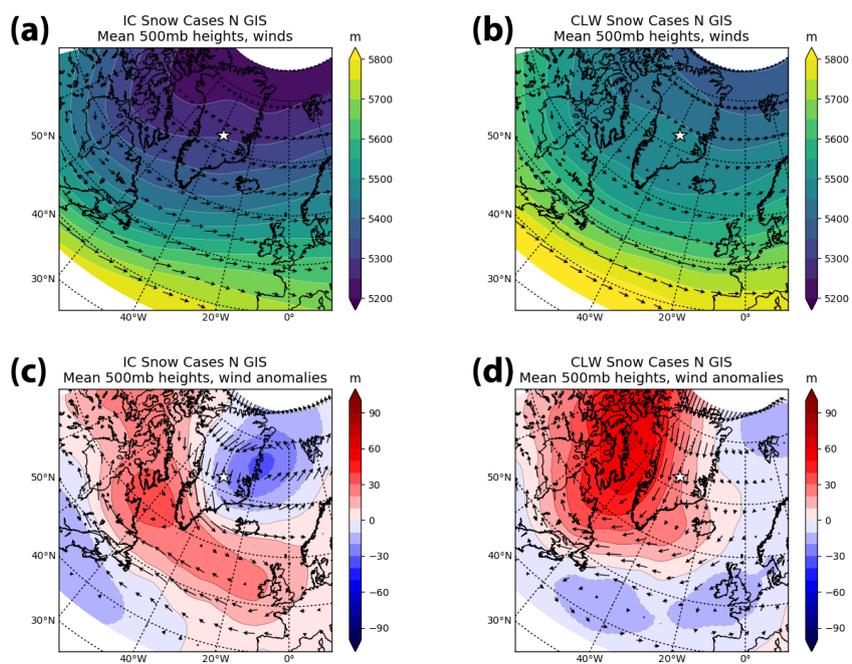
Figure 12. As in Fig. 11 for the northern GIS: basins 1.1, 1.2, 1.3, and 1.4.
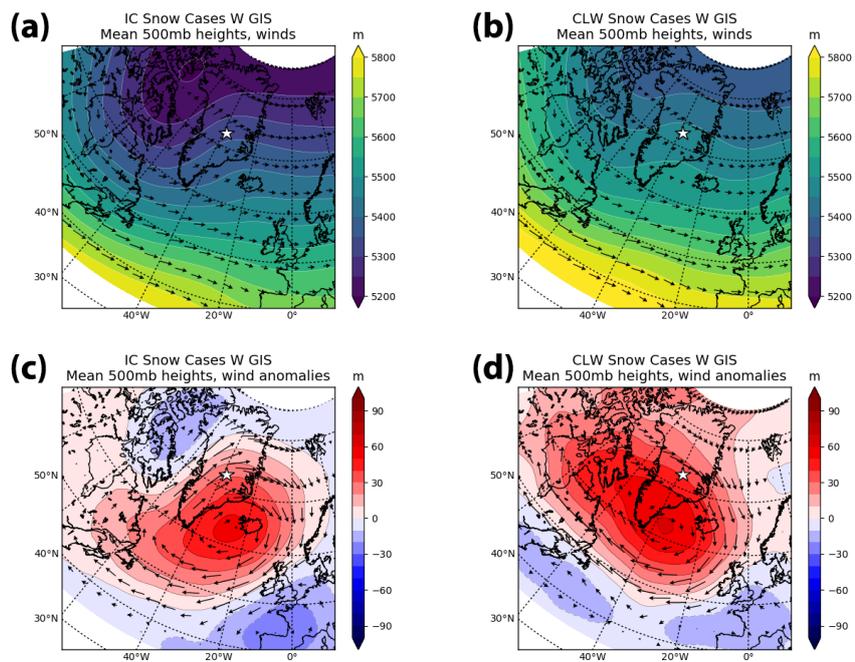
Figure 13. As in Fig. 11 for the western GIS: basins 6.1, 6.2, 7.1, 7.2, 8.1, and 8.2.
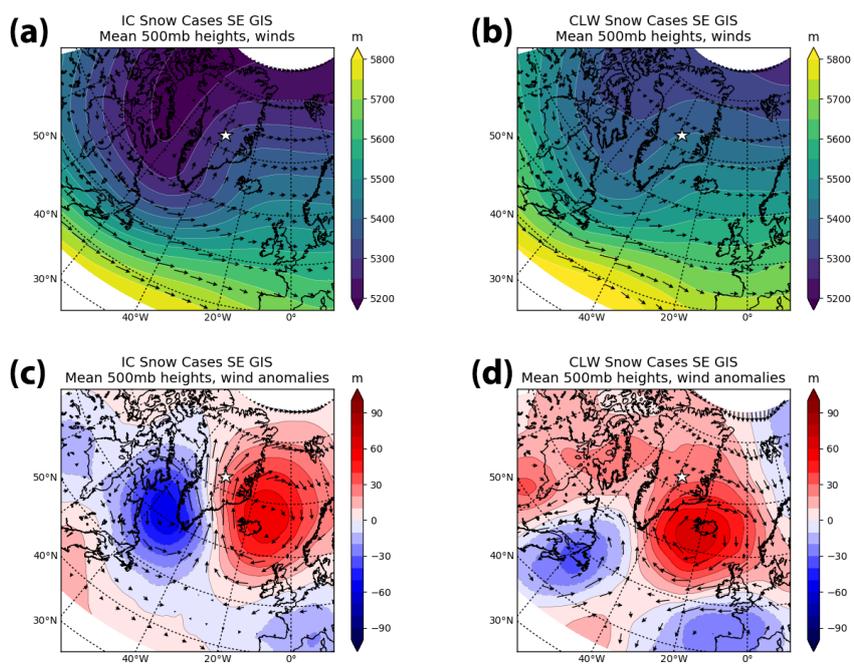
Figure 14. As in Fig. 11 for the southeastern GIS: basins 3.3, 4.1, 4.2, 4.3, and 5.0.

Table 1. Summary of CloudSat snowfall detection capability over Summit Station, Greenland based on averaged MMCR data for POSS detected snowfall. To mimic CloudSat detection we used: a height range of 960-1200 m, equivalent to the standard height of bin 5 of the CPR used in the 2CSP algorithm over land; and time average of 300 s, which at a moderate wind speed of 5 m s^{-1} is equivalent to the horizontal CPR footprint of ∼1.5 km.

Snowfall Event Type	# of Events	Total Fraction Missed	Mean Rate - Missed	Mean Rate - Detected
Total Snow Events	20,516	0.22	0.05	0.09
IC Only Events	3,545	0.05	0.05	0.10
CLW Only Events	9,777	0.25	0.05	0.10

Analysis of CPR-like MMCR reflectivities.

The Cryosphere
Discussions

Open Access

EGU

Table 2. Summary of 2CSP accumulation estimates by GIS basin. All masses are in Gt yr^{-1}. The "summit100" basin includes every observation within 100km of Summit Station.

Basin #	Annual Mass (IC%,CLW%)	Winter Mass (IC%,CLW%)	Summer Mass (IC%,CLW%)	Area km^2
1.1	12 (77 , 23)	4 (88 , 11)	8 (62 , 38)	131,115
1.2	7 (78 , 22)	2 (87 , 13)	4 (67 , 33)	63,773
1.3	5 (83 , 17)	2 (90 , 10)	3 (74 , 26)	46,152
1.4	2 (79 , 21)	1 (87 , 13)	1 (67 , 33)	17,536
2.1	29 (82 , 18)	11 (91 , 9)	17 (71 , 29)	274,220
2.2	6 (85 , 15)	3 (91 , 9)	4 (76 , 24)	51,196
3.1	23 (87 , 13)	9 (94 , 6)	14 (78 , 22)	148,090
3.2	14 (81 , 19)	8 (89 , 11)	6 (70 , 30)	35,619
3.3	31 (86 , 14)	18 (92 , 8)	13 (78 , 22)	73,232
4.1	30 (84 , 16)	18 (90 , 10)	12 (76 , 24)	64,669
4.2	30 (77 , 23)	20 (85 , 15)	10 (67 , 33)	46,802
4.3	24 (73 , 27)	18 (80 , 20)	6 (64 , 36)	33,326
5.0	30 (77 , 23)	18 (85 , 15)	12 (64 , 36)	49,738
6.1	19 (79 , 21)	9 (87 , 13)	10 (67 , 33)	49,909
6.2	36 (78 , 22)	18 (86 , 14)	18 (66 , 34)	136,902
7.1	24 (83 , 17)	11 (92 , 8)	13 (70 , 30)	95,213
7.2	30 (84 , 16)	12 (91 , 9)	18 (73 , 27)	130,027
8.1	42 (82 , 18)	14 (90 , 10)	28 (71 , 29)	241,556
8.2	6 (74 , 26)	2 (85 , 15)	4 (59 , 41)	33,497
summit100	3 (83 , 17)	1 (93 , 7)	2 (69 , 31)	31,416

Summary of snow accumulation by basin.